



Calculation of predictions for non-identical particle correlations in heavy ions collisions at LHC energies from hydrodynamics-inspired models

MASTER OF SCIENCE THESIS

Author:
Mateusz Wojciech Gałażyn

Supervisor:
Prof. Adam Kisiel

Warsaw, 8th December 2014



Wyznaczenie przewidywań teoretycznych dla korelacji cząstek nieidentycznych w zderzeniach ciężkich jonów przy energiach LHC w modelach opartych na hydrodynamice

PRACA MAGISTERSKA

Autor:
Mateusz Wojciech Gałażyn

Promotor:
dr hab. inż. Adam Kisiel, prof. PW

Warszawa, 8 grudnia 2014

1 Abstract

2 This thesis presents results of two-particle momentum correlations analysis
3 for different kinds of particles produced in heavy ion collisions. The studies
4 were carried for the data from lead-lead collisions at the centre of mass energy
5 $\sqrt{s_{NN}} = 2.76$ TeV simulated in the THERMINATOR model using the (3+1)-dimen-
6 sional hydrodynamic model with viscosity. Analysis was performed for the three
7 particle types: pions, kaons and protons for the collisions in eight different cent-
8 rality ranges.

9 The THERMINATOR model allows to perform statistical hadronization of
10 stable particles and unstable resonances from a given hypersurface which is
11 followed by the resonance propagation and decay phase. The four-dimensional
12 hypersurface is coming from the calculations performed on a basis of relativistic
13 hydrodynamic framework with the viscosity corrections.

14 One can investigate space-time characteristics of the particle-emitting source
15 through two-particle interferometry using experimental observables. The
16 experimental-like analysis of the data coming from a model calculations yields
17 a possibility to test the hydrodynamic description of a quark-gluon plasma.
18 This thesis concentrates on the verification of the prediction of appearance of
19 femtoscopic radii scaling with the transverse mass.

20 The three dimensional correlation functions were calculated using spherical
21 harmonics decomposition. One can use this approach to perform calculations
22 with lower statistics and moreover the visualization of results is much easier.
23 The calculated correlation functions show expected increase of a correlation for
24 pions and kaons at the low relative momenta of a pair. For the protons at the
25 same momentum region, the decrease occurs. Furthermore, the transverse pair
26 momentum and centrality dependence on a correlation function is observed. In
27 order to perform the quantitative analysis of this influence, the fitting of the-
28 retical formula for correlation function was performed. The femtoscopic radii
29 calculated in the LCMS and PRF are falling with the transverse mass m_T . To test
30 the scaling predicted from the hydrodynamics, the power law was fitted $\alpha m_T^{-\beta}$.
31 The radii calculated for pions, kaons and protons in the LCMS are following the
32 common scaling. In the case of the PRF such scaling is not observed. To recover
33 the scaling in the PRF, the approximate factor is proposed: $\sqrt{(\sqrt{\gamma_T} + 2)/3}$. The
34 radii in the PRF divided by the proposed scaling factor are falling on the common
35 curve, proving that the scaling can be recovered using the proposed factor. The
36 experimental analysis is usually performed in the PRF (requires less statistics),
37 hence the method of scaling recovery enables easier testing of the hydrodynamic
38 predictions, which are not visible in the PRF.

Streszczenie

W tej pracy zaprezentowane są wyniki analizy dwucząstkowych korelacji pędowych dla trzech różnych typów cząstek produkowanych w zderzeniach ciężkich jonów. Obliczenia zostały wykonane dla danych ze zderzeń ołów-ołów przy energii w centrum masy $\sqrt{s_{NN}} = 2.76$ TeV wygenerowanych za pomocą modelu THERMINATOR przy użyciu (3+1)-wymiarowego modelu hydrodynamicznego uwzględniającego lepkość ośrodka. Analiza została wykonana dla trzech rodzajów cząstek: pionów, kaonów i protonów dla dziewięciu różnych przedziałów centralności.

Model THERMINATOR pozwala na wykonanie statystycznej hadronizacji stabilnych cząstek jak i również niestabilnych rezonansów z danej hiperpowierzchni wymrażania, a następnie uwzględnienie propagacji i rozpadów tych rezonansów. Czterowymiarowa hiperpowierzchnia pochodzi z obliczeń przeprowadzonych na podstawie hydrodynamiki relatywistycznej z uwzględnieniem poprawek pochodzących od lepkości.

Interferometria dwucząstkowa pozwala na zbadanie charakterystyk czasowo-przestrzennych źródła cząstek. Poprzez analizę danych pochodzących z obliczeń modelowych można dokonać sprawdzenia zakresu stosownalności hydrodynamiki do opisu właściwości plazmy kwarkowo-gluonowej. Ta praca koncentruje się na weryfikacji skalowania promieni femtoskopowych z masą poprzeczną przewidywanego przez hydrodynamikę.

Wyliczone trójwymiarowe funkcje korelacyjne zostały rozłożone w szereg harmonik sferycznych. To podejście wymaga mniejszej statystyki i pozwala na łatwiejszą wizualizację wyników. Wyliczone funkcje wykazują oczekiwany wzrost korelacji dla niskich różnic pędów dla par pionów i kaonów. Z kolei dla par protonów w tym samym zakresie pędów można zauważać wyraźny spadek korelacji. Przy czym, we wszystkich przypadkach zderzeń jest widoczny wpływ pędu poprzecznego pary oraz centralności na funkcję korelacyjną. W celu wykonania analizy ilościowej tego wpływu, zostało wykonane dopasowanie formuły analitycznej do obliczonych funkcji korelacyjnych. Otrzymane w ten sposób promienie femtoskopowe w LCMS i PRF wykazują spadek wraz z wzrostem masy poprzecznej m_T . W celu sprawdzenie skalowania przewidywanego przez hydrodynamikę została dopasowana zależność potęgowa: $\alpha m_T^{-\beta}$. Promienie obliczone dla pionów, kaonów i protonów zachowują wzajemne skalowanie w LCMS. W przypadku PRF skalowanie nie jest widoczne, więc aby je odzyskać został zaproponowany przybliżony współczynnik skalowania w postaci: $\sqrt{(\sqrt{\gamma_T} + 2)/3}$. Promienie w PRF po podzieleniu przez tą wartość, dają się opisać oczekowaną zależnością potęgową.

⁷⁷ Analiza eksperimentalna jest zazwyczaj wykonywana w PRF, bowiem wy-
⁷⁸ maga w tym układzie odniesienia mniejszej statystyki. Zatem metoda odzyska-
⁷⁹ nia skalowania pozwala na łatwiejszą, w porównaniu z LCMS, weryfikację prze-
⁸⁰ widywania hydrodynamiki, które nie są widoczne w PRF.

⁸¹ Contents

⁸²	Introduction	1
⁸³	1 Theory of heavy ion collisions	3
⁸⁴	1.1 The Standard Model	3
⁸⁵	1.2 Quantum Chromodynamics	4
⁸⁶	1.2.1 Quarks and gluons	4
⁸⁷	1.2.2 Quantum Chromodynamics potential	5
⁸⁸	1.2.3 The quark-gluon plasma	7
⁸⁹	1.3 Relativistic heavy ion collisions	9
⁹⁰	1.3.1 Stages of heavy ion collision	9
⁹¹	1.3.2 QGP signatures	11
⁹²	2 Therminator model	19
⁹³	2.1 (3+1)-dimensional viscous hydrodynamics	19
⁹⁴	2.2 Statistical hadronization	20
⁹⁵	2.2.1 Cooper-Frye formalism	21
⁹⁶	2.3 Events generation procedure	22
⁹⁷	3 Particle interferometry	25
⁹⁸	3.1 HBT interferometry	25
⁹⁹	3.2 Theoretical approach	25
¹⁰⁰	3.2.1 Conventions used	26
¹⁰¹	3.2.2 Two particle wave function	27
¹⁰²	3.2.3 Source emission function	28
¹⁰³	3.2.4 Analytical form of a correlation function	30
¹⁰⁴	3.2.5 Spherical harmonics decomposition of a correlation function	31
¹⁰⁵	3.3 Experimental approach	32
¹⁰⁶	3.4 Scaling of femtoscopic radii	33
¹⁰⁷	3.4.1 Scaling in LCMS	34
¹⁰⁸	3.4.2 Scaling in PRF	35
¹⁰⁹	4 Results	36
¹¹⁰	4.1 Identical particles correlations	36
¹¹¹	4.1.1 Spherical harmonics components	36

112	4.1.2	Centrality dependence of a correlation function	40
113	4.1.3	k_T dependence of a correlation function	41
114	4.2	Results of the fitting procedure	42
115	4.2.1	The three-dimensional femtoscopic radii scaling	43
116	4.2.2	Scaling of one-dimensional radii	46
117	4.3	Discussion of the results	47
118	Conclusions		48
119	A Correlation function calculation scripts		50
120	A.1	Events generation	50
121	A.2	Calculations of experimental-like correlation functions	51
122	B Fitting utilities		52
123	B.1	Minuit package	52
124	B.2	Fitting software	52
125	B.2.1	Input parameters	52
126	B.2.2	Output format	54
127	B.2.3	Compilation	54
128	B.2.4	Usage	54
129	C Plotting scripts		56
130	C.1	Correlation functions plots	56
131	C.2	Plots with femtoscopic radii	56

¹³² Introduction

Many people were trying to discover what was in the beginning of the Universe which we observe today. Through the years, more or less successful theories were appearing and trying to describe its origin and behaviour. Among them is one model, which provides a comprehensive explanation for a broad range of phenomena, including the cosmic microwave background, abundance of the light elements and Hubble's law. This model is called The Big Bang theory and has been born in 1927 on the basis of the principles proposed by the Belgian priest and scientist Georges Lemaître. Using this model and known laws of physics one can calculate the characteristics of the Universe in detail back in time to the extreme densities and temperatures. However, at some point these calculations fail. The extrapolation of the expansion of the Universe backwards in time using general relativity yields an infinite density and temperature at a finite time in the past. This appearance of singularity is a signal of the breakdown of general relativity. The range of this extrapolation towards singularity is debated - certainly we can go no closer than the end of *Planck epoch* i.e. 10^{-43} s. At this very first era the temperature of the Universe was so high, that the four fundamental forces: electromagnetism, gravitation, weak nuclear interaction and strong nuclear interaction were one fundamental force. Between 10^{-43} s and 10^{-36} s of a lifetime of the Universe, there is a *grand unification epoch*, at which forces are starting to separate from each other. The *electroweak epoch* lasted from 10^{-36} s to 10^{-12} s, when the strong force separated from the electroweak force. After this epoch, there was the *quark epoch* in which the Universe was a dense "soup" of quarks. During this stage the fundamental forces of gravitation, electromagnetism, strong and weak interactions had taken their present forms. The temperature at this moment was still too high to allow quarks to bind together and form hadrons. At the end of quark era, there was a big freeze-out - when the average energy of particle interactions had fallen below the binding energy of hadrons. This era, in which quarks became confined into hadrons, is known as the *hadron epoch*. At this moment the matter had started forming nuclei and atoms, which we observe today.

Here arises the question: how can we study the very beginning of the Universe? To do this, one should recreate in a laboratory appropriate conditions i.e. such large density and high temperature. Today, this is achievable through sophisticated machines like particle accelerators. Sufficiently high energies are available at the Large Hadron Collider at CERN, Geneva and Relativistic Heavy Ion

167 Collider at Brookhaven National Laboratory in Upton, New York. In the particle
168 accelerators the heavy ions after being accelerated to near the speed of light are
169 collided in order to generate extremely dense and hot phase of matter and re-
170 create the quark-gluon plasma. The plasma is believed to behave like an almost
171 ideal fluid, which can be described by the laws of relativistic hydrodynamics.

172 This thesis is providing predictions for collective behaviour of the quark-
173 gluon plasma coming from the hydrodynamic equations. Experimental-like
174 analysis was performed for the high energy Pb-Pb collisions generated with
175 THERMINATOR model.

176 The 1st chapter is an introduction to the theory of heavy ion collisions. It
177 contains the brief description of the Standard Model and Quantum Chromody-
178 namics. Moreover the quark-gluon plasma and its signatures are also here char-
179 acterized.

180 In the 2nd chapter, the relativistic hydrodynamic framework and the
181 THERMINATOR model used to perform the simulations of collisions are
182 described.

183 The 3rd chapter covers the particle interferometry method used in this work.
184 Here are also presented predictions coming from the hydrodynamics, visible in
185 the experimental results. An algorithm of building experimental correlation func-
186 tions is described as well.

187 In the 4th chapter, an interpretation of the results for two-particle femtoscopy
188 for different pairs of particles is presented. Moreover, the quantitative analysis of
189 calculated femtoscopic radii as well as the appearance of transverse mass scaling
190 is discussed.

191 In the Appendices, the detailed description of the tools developed by the au-
192 thor and used in this work is given. Utilities for managing the event generation
193 process and plotting of correlation functions are presented. Furthermore, the fit-
194 ting software, its design and usage is described.

¹⁹⁵ **Chapter 1**

¹⁹⁶ **Theory of heavy ion collisions**

¹⁹⁷ **1.1 The Standard Model**

¹⁹⁸ In the 1970s, a new theory of fundamental particles and their interaction
¹⁹⁹ emerged. It was a new concept, which combines the electromagnetic, weak and
²⁰⁰ strong nuclear interactions between known particles. This theory is called *The*
²⁰¹ *Standard Model*. There are seventeen named particles in the standard model, or-
²⁰² ganized into the chart shown below (Fig. 1.1). Fundamental particles are divided
into two families: *fermions* and *bosons*.

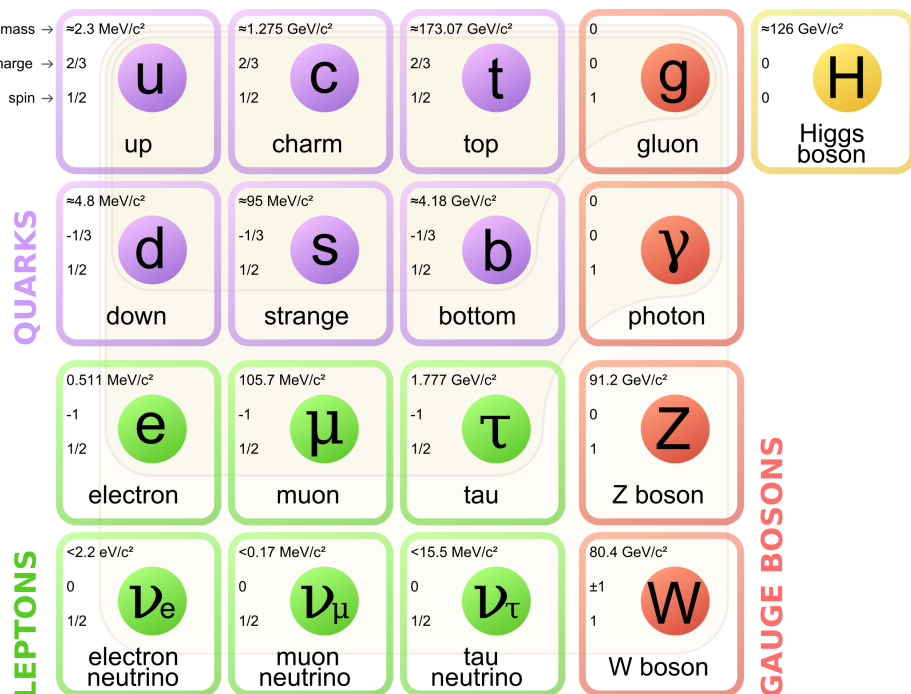


Figure 1.1: The Standard Model of elementary particles [1].

203 Fermions are the building blocks of matter. They are divided into two groups.
 204 Six of them, which must bind together are called *quarks*. Quarks are known to
 205 bind into doublets (*mesons*), triplets (*baryons*) and recently confirmed four-quark
 206 states¹. Two of baryons, with the longest lifetimes, are forming a nucleus: a pro-
 207 ton and a neutron. A proton is build from two up quarks and one down, and
 208 neutron consists of two down quarks and one up. The first one is found to be a
 209 stable particle (at least it has a lifetime larger than 10^{35} years) while a free neutron
 210 has a mean lifetime about 8.8×10^2 s. Fermions that can exist independently are
 211 called *leptons*. Neutrinos are a subgroup of leptons, which are only influenced
 212 by weak interaction. In principle, fermions can be divided into three genera-
 213 tions (three columns in the Figure 1.1). Generation I particles can combine into
 214 hadrons with the longest life spans. Generation II and III consists of unstable
 215 particles which also form unstable hadrons.

216 In turn, bosons are force carriers. There are four fundamental forces: weak -
 217 responsible for radioactive decay, strong - coupling quarks into hadrons, electro-
 218 magnetic - between charged particles and gravity - the weakest, which causes the
 219 attraction between particles with mass. The Standard Model describes the first
 220 three ones. The weak force is mediated by W^\pm and Z^0 bosons, electromagnetic
 221 force is carried by photons γ and the carriers of a strong interaction are gluons
 222 g . Finally, the fifth boson is a Higgs boson which is responsible for giving other
 223 particles mass.

224 1.2 Quantum Chromodynamics

225 1.2.1 Quarks and gluons

226 Quarks interact with each other through the strong interaction. The medi-
 227 ator of this force is a *gluon* - a massless and electrical chargeless particle. In the
 228 quantum chromodynamics (QCD) - theory describing strong interaction - there
 229 are six types of "charges" (like electrical charges in the electrodynamics) called
 230 *colours*. The colours were introduced because some of the observed particles,
 231 like Δ^- , Δ^{++} and Ω^- appeared to consist of three quarks with the same flavour
 232 (ddd , uuu and sss respectively), which was in conflict with the Pauli principle.
 233 One quark can carry one of the three colours (usually called *red*, *green* and *blue*)
 234 while antiquark one of the three anti-colours respectively. Only colour-neutral
 235 (or white) particles could exist. Mesons are assumed to be a colour-anticolour
 236 pair, while baryons are *red-green-blue* triplets. Gluons also are colour-charged
 237 and there are 8 types of gluons. Therefore they can interact with themselves [3].

¹The LHCb experiment at CERN in Geneva confirmed recently the existence of $Z(4430)$ - a particle consisting of four quarks [2].

238 **1.2.2 Quantum Chromodynamics potential**

239 As a result of the fact that gluons are massless, one can expect, that the static
 240 potential in QCD will have the form like similar one in electrodynamics e.g.
 241 $\sim 1/r$ (by analogy to photons). In reality the QCD potential is assumed to have
 242 the form of [3]:

$$V_s = -\frac{4}{3} \frac{\alpha_s}{r} + kr, \quad (1.1)$$

243 where the α_s is a coupling constant of the strong force and the kr part is related
 244 with *confinement*. In comparison to the electromagnetic force, a value of the strong
 245 coupling constant is $\alpha_s \approx 1$ and the electromagnetic one is $\alpha = 1/137$.

246 The fact that quarks does not exist separately and are always bound, is called
 247 confinement. As two quarks are pulled apart, the linear part kr in the Eq. 1.1
 248 becomes dominant and the potential becomes proportional to the distance. This
 249 situation resembles stretching of a string. At some point, when the string is so
 250 large it is energetically favourable to create a quark-antiquark pair. After form-
 251 ation of such pair (or pairs), the string breaks and the confinement is preserved
 (Fig. 1.2).

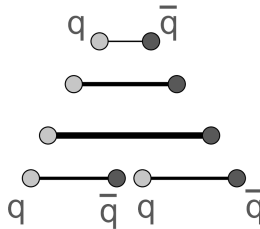


Figure 1.2: A string breaking and a creation of a new quark-antiquark pair [4].

252
 253 On the other hand, for small r , an interaction between the quarks and gluons
 254 is dominated by the Coulomb-like term $-\frac{4}{3} \frac{\alpha_s}{r}$. The coupling constant α_s depends
 255 on the four-momentum Q^2 transferred in the interaction. This dependence is
 256 presented in Fig. 1.3. The value α_s decreases with increasing momentum trans-
 257 fer and the interaction becomes weak for large Q^2 , i.e. $\alpha_s(Q) \rightarrow 0$. Because of
 258 the weakening of coupling constant, quarks at large energies (or small distances)
 259 are starting to behave like free particles. This phenomenon is known as *asym-
 260 ptotic freedom*. The QCD potential exhibits also a temperature dependence - the
 261 force strength "melts" with the temperature increase. Therefore the asymptotic
 262 freedom is expected to appear in either the case of high baryon densities (small
 263 distances between quarks) or very high temperatures. This temperature depend-
 264 ence is illustrated in Fig. 1.4.

265 If the coupling constant α_s is small, one can use perturbative methods to cal-
 266 culate physical observables. Perturbative QCD (pQCD) successfully describes
 267 hard processes (with large Q^2) such as jet production in high energy proton-
 268 antiproton collisions. The applicability of pQCD is defined by the *scale para-
 269 meter* $\Lambda_{QCD} \approx 200$ MeV. If $Q \gg \Lambda_{QCD}$ then the process is in the perturbative



Figure 1.3: The coupling parameter α_s dependence on four-momentum transfer Q^2 [5].

domain and can be described by pQCD. A description of soft processes (when $Q < 1$ GeV) is a problem in QCD - perturbative theory breaks down at this scale. Therefore, to describe reactions with low Q^2 , one has to use alternative methods like Lattice QCD. Lattice QCD (LQCD) is non-perturbative implementation of a field theory in which QCD quantities are calculated on a discrete space-time grid. LQCD allows to obtain properties of matter in equilibrium, but there are some limitations. First of all, Lattice QCD requires fine lattice spacing to obtain precise results. Therefore large computational resources are necessary. However, nowadays with the constant growth of computing power this problem will become less important. The second problem is that lattice simulations are possible only for baryon density $\mu_B = 0$. At $\mu_B \neq 0$, Lattice QCD breaks down because of the sign problem. In QCD the thermodynamic observables are related to the grand canonical partition function, which has a baryonic chemical potential μ_B as a parameter. Therefore, the baryonic density can be controlled by tuning the baryonic chemical potential. For fermions μ_B can be both positive and negative. For particles with μ_B , their antiparticles have chemical potentials with opposite sign $-\mu_B$. Since at the early universe the number of baryons and antibaryons were almost equal we can use $\mu_B = 0$ to a very good approximation [6].

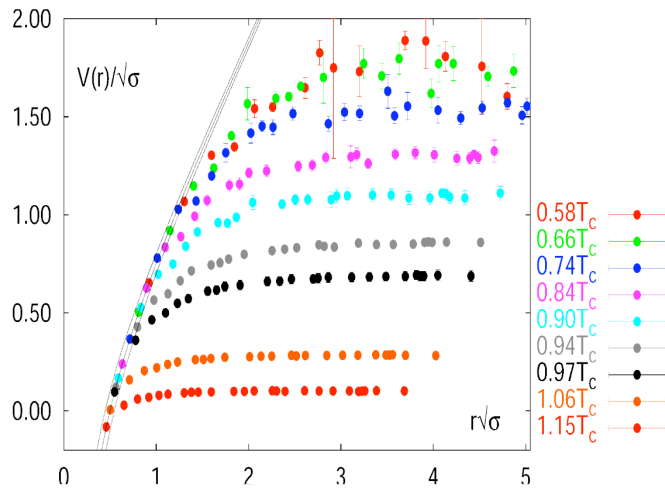


Figure 1.4: The QCD potential for a quark-antiquark pair as a function of distance for different temperatures. A value of a potential decreases with the temperature [4].

288 1.2.3 The quark-gluon plasma

289 The new state of matter in which quarks are no longer confined is known as
290 a *quark-gluon plasma* (QGP). The predictions coming from the discrete space-time
291 Lattice QCD calculations reveal a phase transition from the hadronic matter to
292 the quark-gluon plasma at the high temperatures and baryon densities. The res-
293 ults obtained from these calculations are shown on Fig. 1.5. The energy density ϵ
294 which is divided by T^4 is a measure of the number of degrees of freedom in the

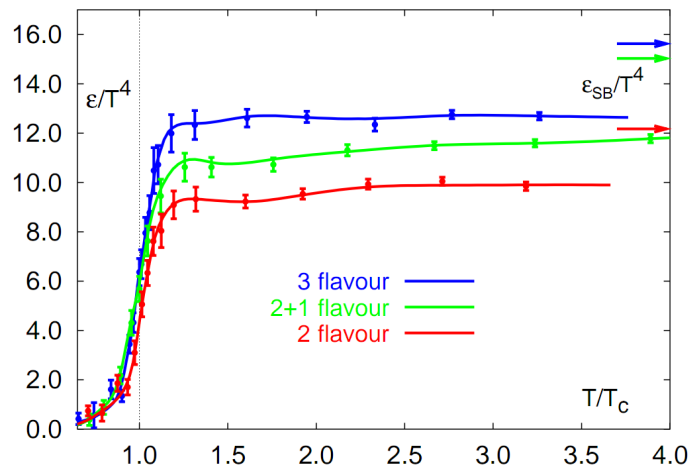


Figure 1.5: A number of degrees of freedom as a function of a temperature [7].

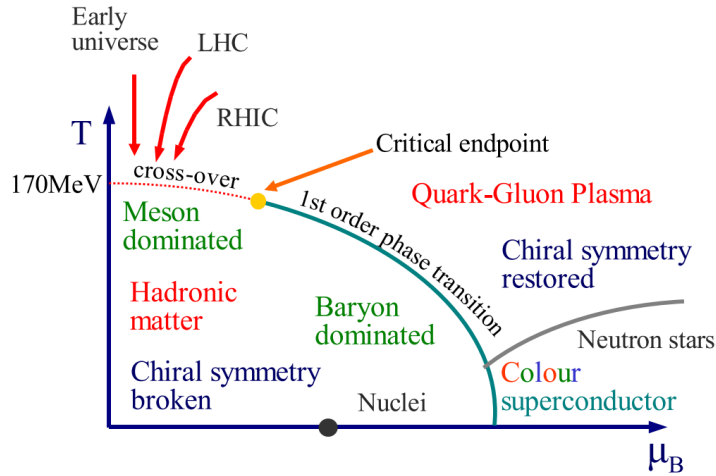


Figure 1.6: Phase diagram coming from the Lattice QCD calculations [8].

system. One can observe significant growth of this value, when the temperature rises past the critical value T_C . Such increase is signaling a phase transition - the formation of QGP [8]. The values of the energy densities plotted in Fig. 1.5 do not reach the Stefan-Boltzmann limit ϵ_{SB} (marked with arrows), which corresponds to an ideal gas. This can indicate some residual interactions in the system. According to the results from the RHIC², the new phase of matter behaves more like an ideal fluid, than like a gas [9].

One of the key questions, to which current heavy ion physics tries to find an answer is the value of a critical temperature T_C as a function of a baryon chemical potential μ_B (baryon density), where the phase transition occurs. The results coming from the Lattice QCD are presented in Fig. 1.6. The phase of matter in which quarks and gluons are deconfined is expected to exist at large temperatures. On the other side, in the region of small temperatures and high baryon densities, a different state is supposed to appear - a *colour superconductor*. The phase transition between hadronic matter and the QGP is thought to be of 1st order at $\mu_B \gg 0$. However as $\mu_B \rightarrow 0$ quarks' masses become significant and a sharp transition transforms into a rapid but smooth cross-over. It is believed that in Pb-Pb collisions observed at the LHC³, the created matter has temperature high enough to be in the quark-gluon plasma phase, then cools down and converts into hadrons, undergoing a smooth transition [8].

²Relativistic Heavy Ion Collider at Brookhaven National Laboratory in Upton, New York

³Large Hadron Collider at CERN, Geneva

315 1.3 Relativistic heavy ion collisions

316 1.3.1 Stages of heavy ion collision

317 To create the quark-gluon plasma one has to achieve sufficiently high tem-
 318 peratures and baryon densities. Such conditions can be recreated in the heavy
 ion collisions at the high energies. The left side of the Figure 1.7 shows simpli-

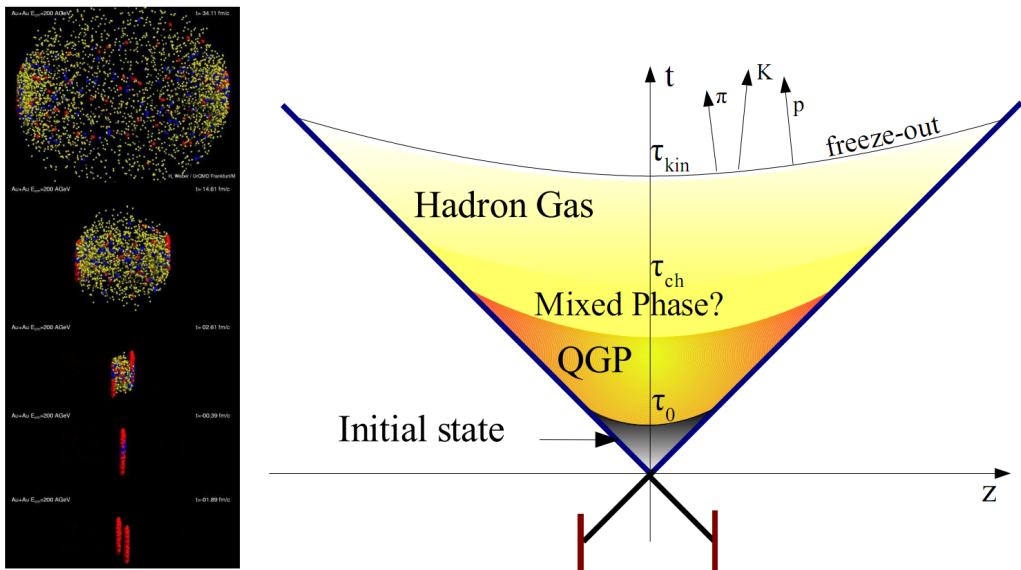


Figure 1.7: Left: stages of a heavy ion collision simulated in the UrQMD model.
 Right: schematic view of a heavy ion collision evolution [8].

319 fied picture of a central collision of two highly relativistic nuclei in the centre-of-
 320 mass reference frame. The colliding nuclei are presented as thin disks because
 321 of the Lorentz contraction. In the central region, where the energy density is the
 322 highest, a new state of matter - the quark-gluon plasma - is supposedly created.
 323 Afterwards, the plasma expands and cools down, quarks combine into hadrons
 324 and their mutual interactions cease when the system reaches the *freeze-out* tem-
 325 perature. Finally, free hadrons created in this process move towards the detectors.
 326

327 On the right side of the Figure 1.7 a space-time evolution of a collision process
 328 is presented, plotted in the light-cone variables (z, t). The two highly relativistic
 329 nuclei are traveling basically along the light cone until they collide at the centre
 330 of the diagram. Nuclear fragments emerge from the collision again along the
 331 (forward) light cone, while the matter between fragmentation zones populates
 332 the central region. This hot and dense matter is believed to be in the state of the
 333 quark-gluon plasma. Nowadays, there are several frameworks describing this
 334 transition to the QGP phase, for example: QCD string breaking, QCD parton
 335 cascades or colour glass condensate evolving into glasma [10].

String breaking – In the string picture, the nuclei pass through each other forming colour strings. This is analogous to the situation depicted in the Fig 1.2 - the colour string is created between quarks inside particular nucleons in nuclei. In the next step strings break forming quarks and gluons or directly hadrons. However, at very high energies, when the strings overlap and cannot be treated as independent objects this approach becomes invalid

Parton cascade – The parton⁴ cascade model is based on the pQCD. The colliding nuclei are treated as clouds of quarks penetrating through each other. The key element of this method is the time evolution of the parton phase-space distributions, which is governed by a relativistic Boltzmann equation with a collision term that contains dominant perturbative QCD interactions. The bottleneck of the parton cascade model is the low energies regime, where the Q^2 is too small to be described by the perturbative theory.

Colour glass condensate – The colour glass condensate assumes, that the hadron can be considered as a tightly packed system of interacting gluons. The saturation of gluons increases with energy, hence the total number of gluons may rise without bound. Such a saturated and weakly coupled gluon system is called a colour glass condensate. The fast gluons in the condensate are Lorentz contracted and redistributed on the two very thin sheets representing two colliding nuclei. These sheets are perpendicular to the beam axis. The fast gluons produce mutually orthogonal colour magnetic and electric fields, that only exist on the sheets. Immediately after the collision, i.e. just after the passage of the two gluonic sheets through each other, the longitudinal electric and magnetic fields are produced forming the *glasma*. The glasma fields decay through the classical rearrangement of the fields into radiation of gluons. Also decays due to the quantum pair creations are possible. In this way, the quark-gluon plasma is also produced.

Interactions within the created quark-gluon plasma bring the system into the local statistical equilibrium, hence its further evolution can be described by the relativistic hydrodynamics. The hydrodynamic expansion causes the system to become more and more dilute. The phase transition from the quark-gluon plasma to the hadronic gas occurs. Further expansion causes a transition from the strongly interacting hadronic gas to weakly interacting system of hadrons which move freely to the detectors. Such decoupling of hadrons is called the *freeze-out*. The freeze-out can be divided into two phases: the chemical freeze-out and the thermal one. The *chemical freeze-out* occurs when the inelastic collisions between constituents of the hadron gas stop. As the system evolves from the chemical freeze-out to the thermal one the dominant processes are elastic collisions (for example $\pi + \pi \rightarrow \rho \rightarrow \pi + \pi$) and strong decays of heavier resonances⁵ which populate the yield of stable hadrons. Thus, the *thermal freeze-out* is the stage of the evolution of matter, when the strongly coupled system transforms to a weakly coupled one (consisting of essentially free particles). In other words

⁴A parton is a common name for a quark and a gluon.

⁵Resonance is other name for an unstable particle.

377 this is the moment, where the hadrons practically stop to interact. Obviously, the
 378 temperatures corresponding to the two freeze-outs satisfy the condition

$$T_{chem} > T_{therm}, \quad (1.2)$$

379 where T_{chem} is the temperature of the chemical freeze-out (inferred from the ratios
 380 of hadron multiplicities), and T_{therm} is the temperature of the thermal freeze-
 381 out (obtained from the investigation of the transverse-momentum spectra) [10].

382 1.3.2 QGP signatures

383 The quark-gluon plasma is a very short living and unstable state of matter.
 384 There is no possibility to investigate the properties of a plasma and confirm
 385 its existence directly. Hence, the several experimental effects were proposed as
 386 QGP signatures, some of them have been already observed in heavy ion experi-
 387 ments [8]. As matter created in the heavy ions collisions is supposed to behave
 388 like a fluid, one should expect appearance of collective behaviour at small trans-
 389 verse momenta - so called *elliptic flow* and *radial flow*. The next signal is the tem-
 390 perature range obtained from the measurements of *direct photons*, which gives us
 391 information that the system created in heavy ion collisions is far above the crit-
 392 ical temperature obtained from the LQCD calculations. The *puzzle in the di-lepton*
 393 *spectrum* can be explained by the modification of spectral shape of vector mesons
 394 (mostly ρ meson) in the presence of a dense medium. This existence of a medium
 395 can also shed light on the *jet quenching* phenomenon - the suppression occurrence
 396 in the high p_T domain.

397 Elliptic flow

398 In a non-central heavy ion collisions, created region of matter has an almond
 399 shape with its shorter axis in the *reaction plane* (Fig. 1.8). The pressure gradient

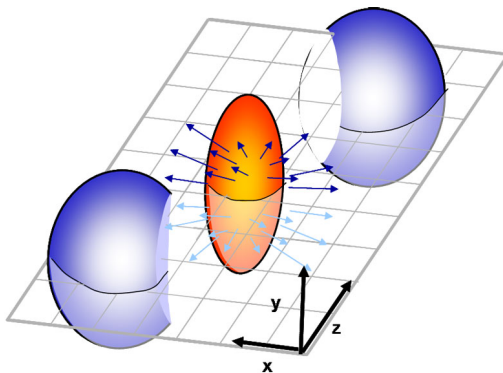


Figure 1.8: Overlapping region which is created in heavy ion collisions has an almond shape. Visible x-z plane is a *reaction plane*. The x-y plane is a *transverse plane*. The z is a direction of the beam [11].

400 is much larger in-plane rather than out-of-plane. Thus, larger acceleration and
 401 transverse velocities are visible in-plane. Such differences can be investigated by
 402 studying the distribution of particles with respect to the reaction plane orienta-
 403 tion [12]:

$$E \frac{d^3 N}{dp^3} = \frac{1}{2\pi} \frac{d^2 N}{p_T dp_T dy} (1 + 2v_1 \cos(\phi) + 2v_2 \cos(2\phi) + \dots), \quad (1.3)$$

404 where ϕ is the angle between particle transverse momentum p_T (a momentum
 405 projection on a transverse plane) and the reaction plane, E is an energy of a
 406 particle and N is their number. The y variable is *rapidity* defined as:

$$y = \frac{1}{2} \ln \left(\frac{E + p_L}{E - p_L} \right), \quad (1.4)$$

407 where p_L is a longitudinal component of a momentum (parallel to the beam direc-
 408 tion). The v_n coefficients indicate the shape of a system. For the most central col-
 409 lisions ($b = 0$ - see Fig. 1.9) all coefficients vanish $\bigwedge_{n \in N_+} v_n = 0$ (the overlapping
 410 region has the spherical shape). The Fourier series elements in the parentheses in
 411 Eq. 1.3 correspond different kinds of flow. The first value "1" represents the *radial*
 412 *flow* - an isotropic flow in every direction. Next coefficient v_1 is responsible for
 413 *direct flow* while the v_2 is a measure of elliptic anisotropy (*elliptic flow*). The v_2 has
 414 to build up in the early stage of a collision - later the system becomes too dilute:
 415 space asymmetry and the pressure gradient vanish. Therefore, the observation
 416 of elliptic flow means that the created matter was in fact a strongly interacting
 417 matter.

418 The v_2 coefficient was already measured at CERN SPS, LHC and RHIC. For
 419 the first time, hydrodynamics successfully described the collision dynamics as

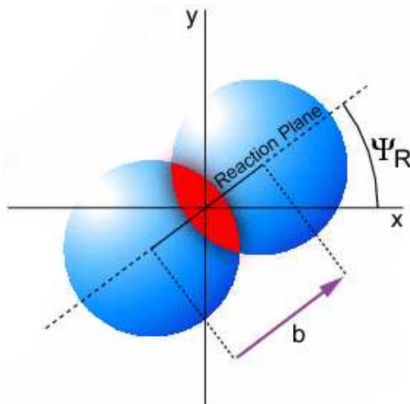


Figure 1.9: Cross-section of a heavy ion collision in a transverse plane. The b parameter is an *impact parameter* - a distance between centers of nuclei during a collision. An impact parameter is related with the centrality of a collision and a volume of the quark-gluon plasma [12].

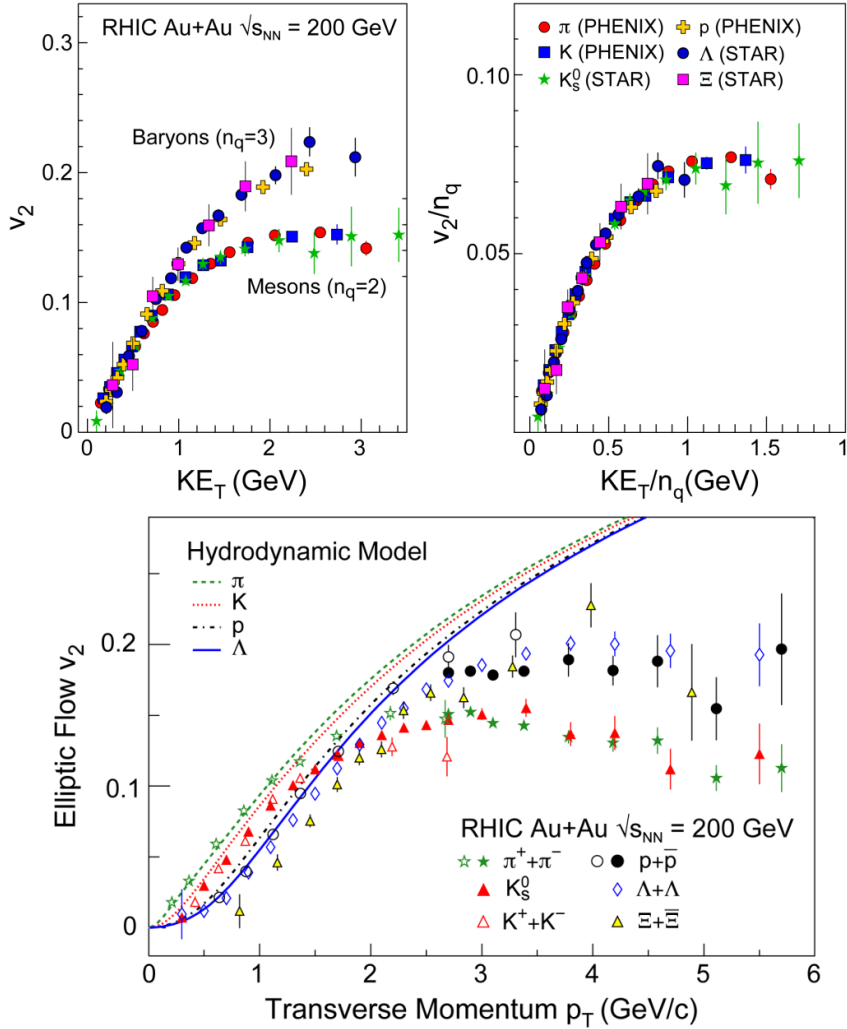


Figure 1.10: *Lower:* The elliptic flow v_2 follows the hydrodynamical predictions for an ideal fluid perfectly. Note that > 99% of all final hadrons have $p_T < 1.5$ GeV/c. *Upper left:* The v_2 plotted versus transverse kinetic energy $KE_T = m_T - m_0 = \sqrt{p_T^2 + m_0^2} - m_0$. The v_2 follows different universal curves for mesons and baryons. *Upper right:* When scaled by the number of valence quarks, the v_2 follows the same universal curve for all hadrons and for all values of scaled transverse kinetic energy [13].

420 the measured v_2 reached hydrodynamic limit (Fig. 1.10). As expected, there is a
 421 mass ordering of v_2 as a function of p_T (lower plot in the Fig. 1.10) with pions
 422 having the largest anisotropy and protons the smallest one. In the upper plots in
 423 the Fig. 1.10 there is a v_2 as a function of transverse kinetic energy. The left plot
 424 shows two universal trend lines for baryons and mesons. After the scaling of v_2

and the kinetic energy by the number of valence quarks, all of the hadrons follow the same universal curve. Those plots prove that strong collectivity is observed in heavy ion collisions.

Transverse radial flow

The elliptic flow, described previously, is caused by the pressure gradient, which must also produce a more simple collective behaviour of matter - a movement inside-out, called radial flow. As a result, particles are pushed to higher momenta and they move away from the center of the collision. A source not showing collective behaviour, like pp collisions, produces particle spectra that can be fitted by a power-law [8]:

$$\frac{1}{2\pi p_T} \frac{d^2N}{dp_T d\eta} = C \left(1 + \frac{p_T}{p_0} \right)^{-n} . \quad (1.5)$$

The η variable is *pseudorapidity* defined as follows:

$$\eta = \frac{1}{2} \ln \left(\frac{p + p_L}{p - p_L} \right) = -\ln \left(\frac{\theta}{2} \right) , \quad (1.6)$$

where θ is an emission angle: $\cos \theta = p_L/p$.

The hydrodynamical expansion of a system gives the same flow velocity kick for different kinds of particles - ones with bigger masses will gain larger p_T boost.

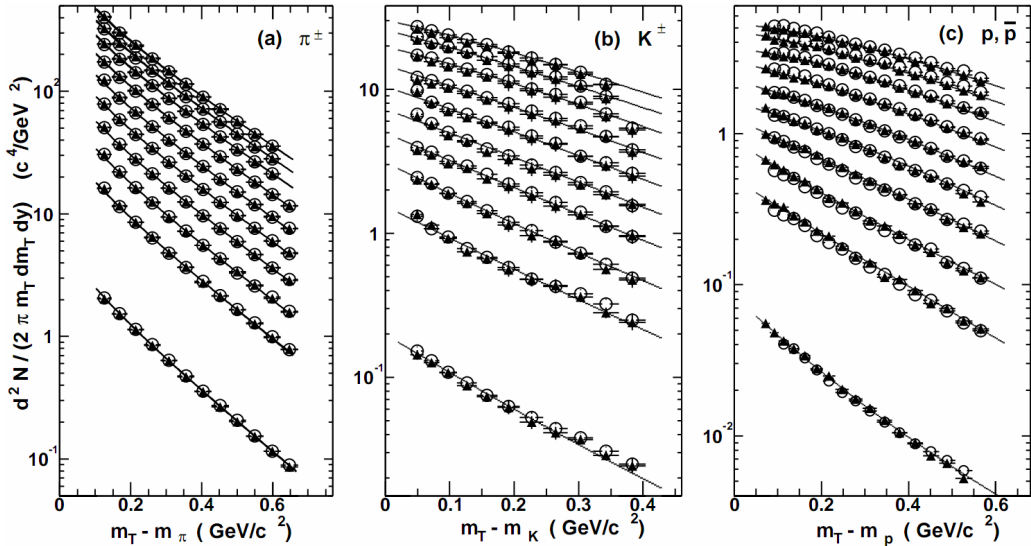


Figure 1.11: Invariant yield of particles versus transverse mass $m_T = \sqrt{p_T^2 + m_0^2}$ for π^\pm , K^\pm , p and \bar{p} at mid-rapidity for p+p collisions (bottom) and Au+Au events from 70-80% (second bottom) to 0-5% (top) centrality [14].

439 This causes increase of the yield of particles with larger transverse momenta. In
 440 the invariant yield plots (Fig. 1.11) one can observe the decrease of the slope para-
 441 meter, especially for the heavier hadrons. The spectra of kaons (b) and protons
 442 (c) are most affected. One can notice decrease of the slope parameter for heavy
 443 ion collisions (plots from second bottom to top) comparing to the proton-proton
 444 collisions (bottom ones), where boost from radial flow should not occur [8].

445 Another signature of a transverse radial flow is a dependence of HBT radii on
 446 a pair transverse momentum. Detailed description of this effect is presented in
 447 Section 3.4.

448 Direct photons

449 The direct photons are photons, which are not coming from the final state
 450 hadrons decays. They can be emitted in different interactions between charged
 451 particles created in the collision, either at the partonic or at the hadronic level.
 452 Direct photons are considered to be an excellent probe of the early stage of the
 453 collision. It is the result of the fact that their mean free path is very large in
 454 comparison to the size of system created in the collision. Thus, photons created
 455 at the early stage leave the system without suffering any interaction and retain
 456 information about this stage, in particular about its temperature.

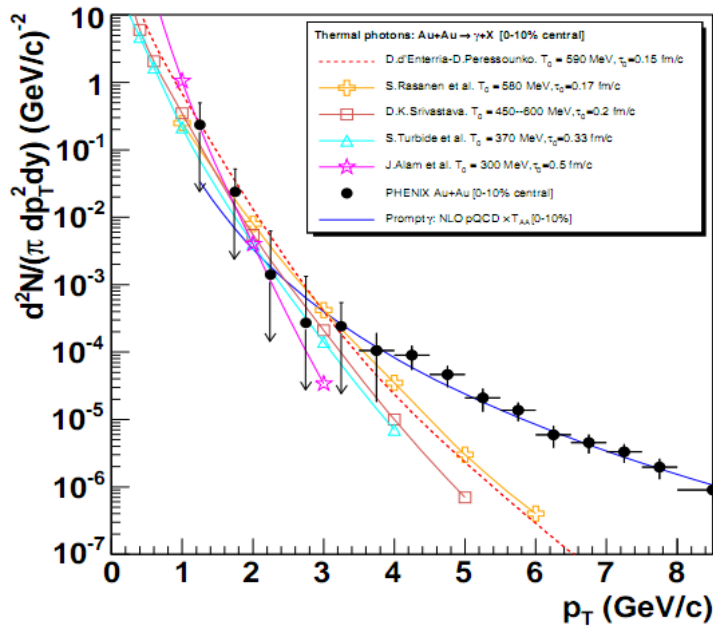


Figure 1.12: Thermal photons spectra for the central Au+Au collisions at $\sqrt{s_{NN}} = 200$ GeV computed within different hydrodynamical models compared with the pQCD calculations (solid line) and experimental data from PHENIX (black dots) [15].

One can distinguish two kinds of direct photons: *thermal* and *prompt*. Thermal photons can be emitted from the strong processes in the quark-gluon plasma involving quarks and gluons or hot hadronic matter (e.g. processes: $\pi\pi \rightarrow \rho\gamma$, $\pi\rho \rightarrow \pi\gamma$). They can be observed in the low p_T region. Prompt photons are believed to come from “hard” collisions of initial state partons belonging to the colliding nuclei. They will dominate the high p_T region and can be described using the pQCD. The analysis of transverse momentum of spectra of direct photons revealed that the temperature of the source of thermal photons produced in heavy ion collisions at RHIC is in the range of 300-600 MeV (Fig. 1.12). Hence, the direct photons had to come from a system whose temperature is far above from the critical temperature for QGP creation.

Puzzle in di-lepton mass spectrum

The invariant mass spectra (Fig. 1.13) of lepton pairs reveal many peaks corresponding to direct decays of various mesons into a lepton pairs. The continuous background in this plot is caused by the decays of hadrons into more than two leptons (including so-called *Dalitz decays* into a lepton pair and a photon). Particular hadron decay channels, which contribute to this spectrum are shown in Fig. 1.13 with the coloured lines. The sum of various components (called “*the hadronic cocktail*”) is represented by the black line. It describes experimental spectra coming from the simple collisions (like p+p or p+A) quite well with the statistical and systematical uncertainties [9]. However, this situation is different considering more complicated systems i.e. A+A. Exemplary spectra coming from

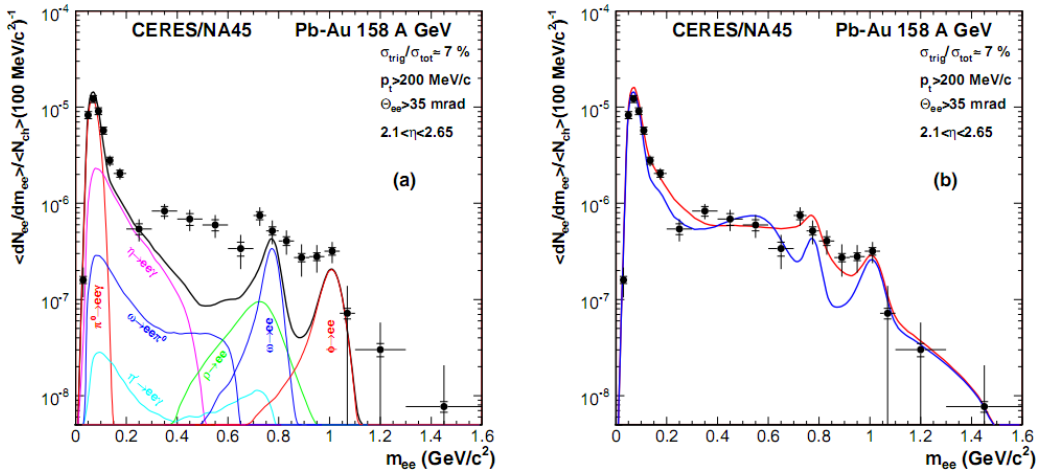


Figure 1.13: Left: Invariant mass spectrum of $e^+ - e^-$ pairs in Pb+Au collisions at 158A GeV compared to the sum coming from the hadron decays predictions. Right: The expectations coming from model calculations which assume a drop of the ρ mass (blue) or a spread of the ρ width in the medium (red) [16].

Pb+Au collisions are presented in the plots in Fig. 1.13. The “hadronic cocktail” does not describe the data in the mass range between the π and the ρ mesons. One can observe a significant excess of electron pairs over the calculated sum in this region. Theoretical explanation of this phenomenon assumes modification of the spectral shape of vector mesons in a dense medium. Two different interpretations of this increase were proposed: a decrease of meson’s mass with the medium density and increase of the meson’s width in the dense medium. In principle, one could think of simultaneous occurrence of both effects: mass shift and resonance broadening. Experimental results coming from the CERES disfavour the mass shift hypothesis indicating only broadening of resonance peaks (Fig. 1.13b) [9].

490 Jet quenching

A jet is defined as a group of particles with high energies and close vector momenta. It has its beginning when the two partons are going in opposite directions and have energy big enough to produce new quark-antiquark pair and then radiate gluons. This process can be repeated many times and as a result two back-to-back jets of hadrons are created. It has been found that jets in the opposite hemisphere (*away-side jets*) show a very different pattern in d+Au and Au+Au collisions. This is presented in the azimuthal correlations in the Fig. 1.14. In d+Au collisions, like in p+p, a pronounced away-side jet appears around $\Delta\phi = \pi$ - exactly opposite to the trigger jet, which is typical for di-jet events. However, in the case of central Au+Au collisions the away-side jet is suppressed. When the

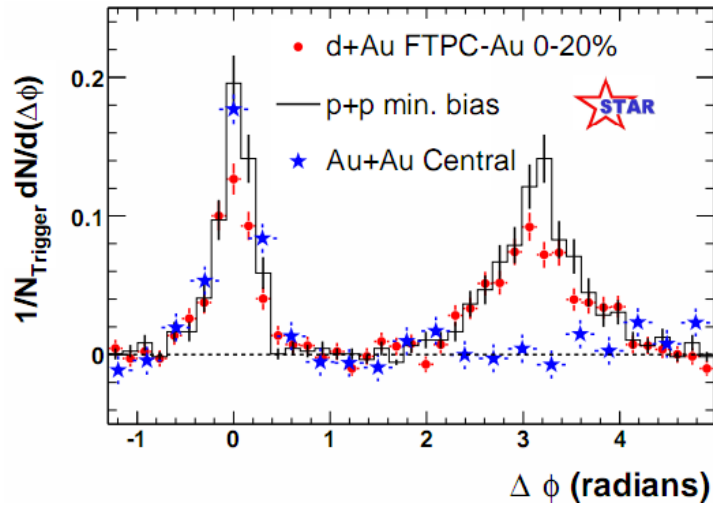


Figure 1.14: Azimuthal angle difference $\Delta\phi$ distributions for different colliding systems at $\sqrt{s_{NN}} = 200$ GeV. Transverse momentum cut: $p_T > 2$ GeV. For the Au+Au collisions the away-side jet is missing [17].

501 jet has its beginning near the surface of the quark-gluon plasma, one of the jets
502 (*near-side jet*) leaves the system almost without any interactions. This jet is visible
503 in the correlation plot as a high peak at $\Delta\phi = 0$. However, the jet which moves
504 towards the opposite direction has to penetrate a dense medium. The interac-
505 tion with the plasma causes energy dissipation of particles and is visible on an
506 azimuthal correlation plot as a disappearance of the away-side jet [9].

507 **Chapter 2**

508 **Therminator model**

509 THERMINATOR [18] is a Monte Carlo event generator designed to investigate
510 the particle production in the relativistic heavy ion collisions. The functionality
511 of the code includes a generation of the stable particles and unstable resonances
512 at the chosen hypersurface model. It performs the statistical hadronization which
513 is followed by space-time evolution of particles and the decay of resonances. The
514 key element of this method is an inclusion of a complete list of hadronic reso-
515 nances, which contribute very significantly to the observables. The second version
516 of THERMINATOR [19] gives a possibility to utilize any shape of freeze-out hyper-
517 surface and the expansion velocity field, especially those generated externally
518 with various hydrodynamic codes. The event generator is written in C++ pro-
519 gramming language and it employs ROOT [20] analysis framework.

520 **2.1 (3+1)-dimensional viscous hydrodynamics**

521 Most of the relativistic viscous hydrodynamic calculations are done in
522 (2+1)-dimensions. Such simplification assumes boost-invariance of a matter
523 created in a collision. Experimental data reveal that no boost-invariant region is
524 formed in the collisions [21]. Hence, for the better description of created system
525 a (3+1)-dimensional model is required.

526 In the four dimensional relativistic dynamics one can describe a system
527 using a space-time four-vector $x^\nu = (ct, x, y, z)$, a velocity four-vector
528 $u^\nu = \gamma(c, v_x, v_y, v_z)$ and a energy-momentum tensor $T^{\mu\nu}$. The particular
529 components of $T^{\mu\nu}$ have a following meaning:

- 530 • T^{00} - an energy density,
- 531 • $cT^{0\alpha}$ - an energy flux across a surface x^α ,
- 532 • $T^{\alpha 0}$ - an α -momentum flux across a surface x^α multiplied by c ,
- 533 • $T^{\alpha\beta}$ - components of momentum flux density tensor,

534 where $\gamma = (1 - v^2/c^2)^{-1/2}$ is a Lorentz factor and $\alpha, \beta \in \{1, 2, 3\}$. $T^{\mu\nu}$ can be
 535 expressed using u^ν as follows [22]:

$$T_0^{\mu\nu} = (e + p)u^\mu u^\nu - pg^{\mu\nu} \quad (2.1)$$

536 where e is an energy density, p is a pressure and $g^{\mu\nu}$ is an inverse metric tensor:

$$g^{\mu\nu} = \begin{bmatrix} 1 & 0 & 0 & 0 \\ 0 & -1 & 0 & 0 \\ 0 & 0 & -1 & 0 \\ 0 & 0 & 0 & -1 \end{bmatrix}. \quad (2.2)$$

537 The presented version of energy-momentum tensor (Eq. 2.1) can be used to de-
 538 scribe dynamics of a perfect fluid. To take into account influence of viscosity,
 539 one has to apply the following corrections coming from shear $\pi^{\mu\nu}$ and bulk Π
 540 viscosities [23]:

$$T^{\mu\nu} = T_0^{\mu\nu} + \pi^{\mu\nu} + \Pi(g^{\mu\nu} - u^\mu u^\nu). \quad (2.3)$$

541 The stress tensor $\pi^{\mu\nu}$ and the bulk viscosity Π are solutions of dynamical equa-
 542 tions in the second order viscous hydrodynamic framework [22]. The compari-
 543 son of hydrodynamic calculations with the experimental results reveals that the
 544 shear viscosity divided by entropy η/s has to be small and close to the AdS/CFT
 545 estimate $\eta/s = 0.08$ [23, 24]. The bulk viscosity over entropy value used in calcu-
 546 lations is $\zeta/s = 0.04$ [23].

547 In the situation, when system described by $T^{\mu\nu}$ is evolving close to local ther-
 548 modynamic equilibrium, then relativistic hydrodynamic equations take the fol-
 549 lowing form:

$$\partial_\mu T^{\mu\nu} = 0, \quad (2.4)$$

550 which can be used to determine the dynamics of the local energy density, pres-
 551 sure and flow velocity.

552 Hydrodynamic calculations are starting from the Glauber¹ model initial con-
 553 ditions. The collective expansion of a fluid ends at the freeze-out hypersurface.
 554 That surface is usually defined as a constant temperature surface, or equivalently
 555 as a cut-off in local energy density. The freeze-out is assumed to occur at the
 556 temperature $T = 140$ MeV.

557 2.2 Statistical hadronization

558 Statistical description of heavy ion collisions has been successfully used to
 559 quantitatively characterize the *soft* physics, i.e. the regime with the transverse
 560 momentum not exceeding 2 GeV. The basic assumption of the statistical approach
 561 of evolution of the quark-gluon plasma is that at some point of the space-time

¹The Glauber Model is used to calculate “geometrical” parameters of a collision like an impact parameter, number of participating nucleons or number of binary collisions.

562 evolution of the fireball, the thermal equilibrium is reached. When the system
 563 is in this state the local phase-space densities of particles follow the Fermi-Dirac
 564 or Bose-Einstein statistical distributions. At the end of the plasma expansion, the
 565 freeze-out occurs. The freeze-out model incorporated in THERMINATOR assumes,
 566 that chemical and thermal freeze-outs occur at the same time.

567 2.2.1 Cooper-Frye formalism

568 The result of the hydrodynamic calculations is the freeze-out hypersurface Σ^μ . A three-dimensional element of the surface is defined as [19]
 569

$$570 \quad d\Sigma_\mu = \epsilon_{\mu\alpha\beta\gamma} \frac{\partial x^\alpha}{\partial \alpha} \frac{\partial x^\beta}{\partial \beta} \frac{\partial x^\gamma}{\partial \gamma} d\alpha d\beta d\gamma, \quad (2.5)$$

571 where $\epsilon_{\mu\alpha\beta\gamma}$ is the Levi-Civita tensor and the variables $\alpha, \beta, \gamma \in \{1, 2, 3\}$ are used
 572 to parametrize the three-dimensional freeze-out hypersurface in the Minkowski
 573 four-dimensional space. The Levi-Civita tensor is equal to 1 when the indices
 574 form an even permutation (eg. ϵ_{0123}), to -1 when the permutation is odd (e.g.
 575 ϵ_{2134}) and has a value of 0 if any index is repeated. Therefore [19],

$$576 \quad d\Sigma_0 = \begin{vmatrix} \frac{\partial x}{\partial \alpha} & \frac{\partial x}{\partial \beta} & \frac{\partial x}{\partial \gamma} \\ \frac{\partial y}{\partial \alpha} & \frac{\partial y}{\partial \beta} & \frac{\partial y}{\partial \gamma} \\ \frac{\partial z}{\partial \alpha} & \frac{\partial z}{\partial \beta} & \frac{\partial z}{\partial \gamma} \end{vmatrix} d\alpha d\beta d\gamma \quad (2.6)$$

576 while the remaining components are obtained by cyclic permutations of t, x, y
 577 and z .

The number of hadrons produced on the hypersurface Σ^μ can be calculated
 from the Cooper-Frye formalism. The following integral yields the total number
 of created particles [19]:

$$577 \quad N = (2s + 1) \int \frac{d^3 p}{(2\pi)^3 E_p} \int d\Sigma_\mu p^\mu f(p_\mu u^\mu) , \quad (2.7)$$

578 where $f(p_\mu u^\mu)$ is the phase-space distribution of particles (for stable ones and
 579 resonances). The dependence of the momentum density can be simply derived
 580 from Eq. 2.7 [25]:

$$580 \quad E \frac{d^3 N}{dp^3} = \int d\Sigma_\mu f(p_\mu u^\mu) p^\mu . \quad (2.8)$$

581 The momentum distribution f contains non-equilibrium corrections:

$$582 \quad f = f_0 + \delta f_{shear} + \delta f_{bulk} , \quad (2.9)$$

582 where

$$583 \quad f_0(p_\mu u^\mu) = \left\{ \exp \left[\frac{p_\mu u^\mu - (B\mu_B + I_3\mu_{I_3} + S\mu_S + C\mu_C)}{T} \right] \pm 1 \right\}^{-1} . \quad (2.10)$$

583 In case of fermions, in the Eq. 2.10 there is a plus sign and for bosons, minus
 584 sign respectively. The thermodynamic quantities appearing in the $f_0(\cdot)$ are
 585 T - temperature, μ_B - baryon chemical potential, μ_{I_3} - isospin chemical potential,
 586 μ_S - strange chemical potential, μ_C - charmed chemical potential and s as a
 587 spin of a particle. The hydrodynamic calculations yield the flow velocity at
 588 freeze-out as well as the stress and bulk viscosity tensors required to calculate
 589 non-equilibrium corrections to the momentum distribution used in Eq. 2.7. The
 590 term coming from shear viscosity has a form [23]

$$\delta f_{shear} = f_0(1 \pm f_0) \frac{1}{2T^2(e+p)} p^\mu p^\nu \pi_{\mu\nu} \quad (2.11)$$

591 and bulk viscosity

$$\delta f_{bulk} = C f_0(1 \pm f_0) \left(\frac{(u^\mu p_\mu)^2}{3u^\mu p_\mu} - c_s^2 u^\mu p_\mu \right) \Pi \quad (2.12)$$

592 where c_s is sound velocity and

$$\frac{1}{C} = \frac{1}{3} \frac{1}{(2\pi)^3} \sum_{hadrons} \int d^3p \frac{m^2}{E} f_0(1 \pm f_0) \left(\frac{p^2}{3E} - c_s^2 E \right). \quad (2.13)$$

593 2.3 Events generation procedure

594 The equations presented in the previous section are directly used in the
 595 THERMINATOR to generate the primordial hadrons (created during freeze-out)
 596 with the Monte-Carlo method. This procedure consists of 3 main steps, where
 597 the first two are performed only once per given parameter set. After the
 598 generation of primordial particles, the cascade decay of unstable resonances is
 599 performed.

600 Determination of a maximum of an integrand

601 In order to generate particles through a Monte Carlo method, the maximum
 602 value of the distribution in the right-hand-side of Eq. 2.7 must be known. To find
 603 this number, THERMINATOR performs generation of a sample consisting of a large
 604 number of particles. For each particle the value of a distribution is calculated
 605 and the maximum value f_{max} of the sample is stored. A large enough sample
 606 of particles guarantees that f_{max} found in this procedure is a good estimate of
 607 the maximum value of a distribution in Eq. 2.7. This maximum value depends
 608 on a particle type and values of parameters, but does not change from event to
 609 event. Hence this procedure is performed once, at the beginning of the events
 610 generation [18].

611 **Multiplicity calculation**

612 In order to generate events, a multiplicity of each particle must be known.
 613 The multiplicities are obtained through a numerical integration of distribution
 614 functions (Eq. 2.7) in the given integration ranges determined by the model para-
 615 meters. As in the previous case, the multiplicities depend only on the model
 616 parameters and they are calculated only once at the beginning of the events gen-
 617 eration [18].

618 **Events and particles generation**

619 Every event produced by THERMINATOR is generated separately. At first, the
 620 multiplicities for each of particle type are calculated as random numbers from a
 621 Poisson distribution, with the mean being the average particles multiplicity de-
 622 termined in the previous step. Then, the program proceeds to generate particles
 623 from the heaviest to the lightest ones. In essence, this procedure is a generation
 624 of the set of six random numbers: three components of particle's momentum (p_x ,
 625 p_y , p_z) and three parameters providing space-time coordinates on a freeze-out
 626 hypersurface (ζ , ϕ_s , θ). The events generation procedure is based on the von
 627 Neumann's acceptance-rejection algorithm. Firstly, the integrand in Eq. 2.7 is
 628 calculated using given set of numbers. Subsequently, a random number from
 629 uniform distribution over $[0; f_{max}]$ is compared to the value of integrand. If it
 630 is lower, then the set of numbers is stored as an actual particle. If this condi-
 631 tion was not satisfied, a new set is generated. This procedure is repeated until
 632 the determined number of particles of each kind is generated. At this point, all
 633 primordial particles (stable and resonances) have been generated and stored in
 634 the event [18].

635 **Decays of unstable particles**

636 In the next step of event generation, a simulation of unstable resonances de-
 637 cays is performed. A particle is considered as unstable when it has non-zero
 638 width Γ defined in the input files of THERMINATOR. The decays proceed sequen-
 639 tially from the heaviest to the lightest particles. Unstable products of decays are
 640 added to the particles generated in the current event and are processed in the
 641 subsequent steps. If a particle has several decay channels, one of them is selec-
 642 ted randomly with the appropriate probability corresponding to the branching
 643 ratio provided in the input files. THERMINATOR in the hadronic cascade process
 644 performs two-body and three-body decays.

645 At the beginning of the cascade decay, the lifetime τ of a particle with mass
 646 M , moving with the four-momentum p^μ , is generated randomly according to the
 647 exponential decay law $\exp(-\Gamma\tau)$. When the lifetime is known, the point of its
 648 decay is calculated as [18]:

$$x_{decay}^\mu = x_{origin}^\mu + \frac{p^\mu}{M}\tau, \quad (2.14)$$

649 where x_{origin}^μ is a position of unstable particle's creation. At the x_{decay}^μ point de-
 650 cay occurs and daughter particles with energies and momenta determined by
 651 the conservation laws are generated. Fig. 2.1 illustrates the cascade decay pro-
 cess [18].

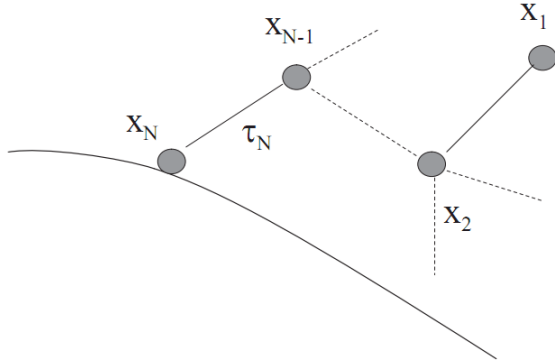


Figure 2.1: The cascade decay in the single freeze-out model. An unstable resonance x_N is formed at the freeze-out hypersurface and travels for the time τ_N depending on its lifetime and decays. If the products are also resonances (x_{N-1}, x_2) they decay further until the stable particles are formed (x_1) [18].

653 **Chapter 3**

654 **Particle interferometry**

655 Two-particle interferometry (also called *femtoscopy*) gives a possibility to
656 investigate space-time characteristics of the particle-emitting source created
657 in heavy ion collisions. Through the study of particle correlations, their
658 momentum distributions can be used to obtain information about the spatial
659 extent of the created system. Using this method, one can measure sizes of the
660 order of 10^{-15} m and time of the order of 10^{-23} s.

661 **3.1 HBT interferometry**

662 In the 1956 Robert Hanbury Brown and Richard Q. Twiss proposed a method
663 which allowed to investigate angular dimensions of stars through analysis of
664 interference between photons. They performed a measurement of the intensity
665 of a beam of light coming from a star using two separated detectors. In a sig-
666 nal plotted as a function of distance between detectors an interference effect was
667 observed, revealing a positive correlation, despite the fact that no phase inform-
668 ation was collected. Hanbury, Brown and Twiss used this interference signal to
669 calculate the angular size of a star with the excellent resolution. This method was
670 designed to be used in astronomy, however HBT interferometry can be used also
671 to measure extent of any emitting source. Therefore it was adapted to heavy ion
672 collisions to investigate dimensions of a particle-emitting source [8].

673 **3.2 Theoretical approach**

674 Intensity interferometry in heavy ion physics uses similar mathematical form-
675 alism as the astronomy HBT measurement. The difference between them is that
676 femtoscopy uses a two-particle relative momentum and yields the space-time
677 picture of a source, whereas the latter method uses the distance between detect-
678 ors to calculate angular size of the star.

679 **3.2.1 Conventions used**

680 In heavy ion collisions to describe particular directions, components of mo-
 681 mentum and location of particles, one uses naming convention called the Bertsch-
 Pratt coordinate system. This system is presented in the Fig. 3.1. The three dir-

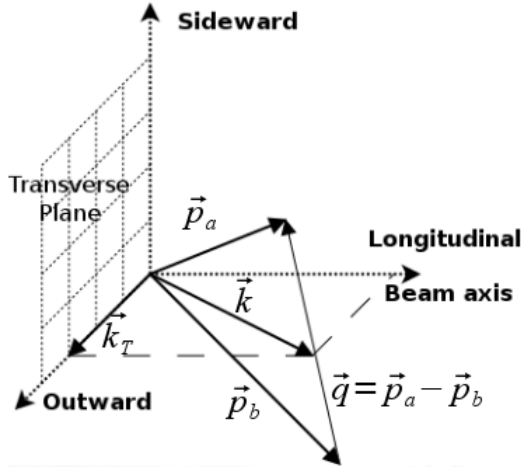


Figure 3.1: Bertsch-Pratt direction naming convention used in heavy ion collision.

682 ections are called *longitudinal*, *outward* and *sideward*. The longitudinal direction
 683 is parallel to the beam axis. The plane perpendicular to the beam axis is called
 684 a *transverse plane*. A projection of a particle pair momentum $\mathbf{k} = (\mathbf{p}_a + \mathbf{p}_b)/2$
 685 on a transverse plane (a *transverse momentum* \mathbf{k}_T) determines *outward* direction:
 686 $(\mathbf{k})_{out} = \mathbf{k}_T$. A direction perpendicular to the longitudinal and outward is called
 687 *sideward*.
 688

689 A particle pair is usually described using two coordinate systems. The first
 690 one, *Longitudinally Co-Moving System* (LCMS) is moving along the particle pair
 691 with the longitudinal direction, in other words, the pair longitudinal momentum
 692 vanishes: $(\mathbf{p}_a)_{long} = -(\mathbf{p}_b)_{long}$. The second system is called *Pair Rest Frame* (PRF).
 693 In the PRF the centre of mass rests: $\mathbf{p}_a = -\mathbf{p}_b$. Variables which are expressed in
 694 the PRF are marked with a star (e.g. \mathbf{k}^*).

The transition of space-time coordinates from LCMS to PRF is simply
 a boost along the outward direction, with the transverse velocity of the
 pair $\beta_T = (\mathbf{v}/c)_{out}$ [26]:

$$r_{out}^* = \gamma_t(r_{out} - \beta_T \Delta t) \quad (3.1)$$

$$r_{side}^* = r_{side} \quad (3.2)$$

$$r_{long}^* = r_{long} \quad (3.3)$$

$$\Delta t^* = \gamma_T(\Delta t - \beta_T r_{out}), \quad (3.4)$$

695 where $\gamma_T = (1 - \beta_T^2)^{-1/2}$ is the Lorentz factor. However, in calculations performed

in this work the equal time approximation is used, which assumes that particles in a pair were produced at the same time in PRF - the Δt^* is neglected.

The most important variables used to describe particle pair are their total momentum $\mathbf{P} = \mathbf{p}_a + \mathbf{p}_b$ and relative momentum $\mathbf{q} = \mathbf{p}_a - \mathbf{p}_b$. In the PRF one has $\mathbf{q} = 2\mathbf{k}^*$, where \mathbf{k}^* is a momentum of the first particle in PRF.

3.2.2 Two particle wave function

Let us consider two identical particles with momenta \mathbf{p}_1 and \mathbf{p}_2 emitted from space points \mathbf{x}_1 and \mathbf{x}_2 . Those emitted particles can be treated as two incoherent waves. If the particles are identical, they are also indistinguishable, therefore one

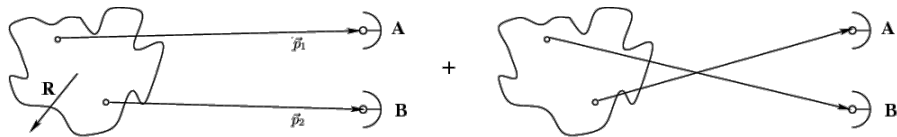


Figure 3.2: The pair wave function is a superposition of all possible states. In case of particle interferometry it includes two cases: particles with momenta p_1, p_2 registered by detectors A, B and p_1, p_2 registered by B, A respectively.

has also take into account the scenario, where the particle with momentum \mathbf{p}_1 is emitted from \mathbf{x}_2 and particle \mathbf{p}_2 from \mathbf{x}_1 (Fig. 3.2). In such case, the wave function describing behaviour of a pair has to contain both components [8]:

$$\Psi_{ab}(\mathbf{q}) = \frac{1}{\sqrt{2}} [\exp(-i\mathbf{p}_1\mathbf{x}_1 - i\mathbf{p}_2\mathbf{x}_2) \pm \exp(-i\mathbf{p}_2\mathbf{x}_1 - i\mathbf{p}_1\mathbf{x}_2)] . \quad (3.5)$$

A two particle wave function of identical bosons is symmetric ("+" sign in Eq. 3.5) and in case of identical fermions - antisymmetric ("-" sign). This anti-symmetrization or symmetrization implies the correlation effect coming from the Fermi-Dirac or Bose-Einstein statistics accordingly.

To provide full description of a system consisting of two charged hadrons, one has to include in the wave function besides quantum statistics also Coulomb and strong Final State Interactions. The aim of this work is an analysis of femtoscopic radii proportional to the inverse of a width of a correlation function (for detailed description see Section 3.2.4). Since we are not interested in the direct comparison of experimental correlation functions with their analytical forms, the following simplification can be made. A width of identical particles correlation function is determined by effects coming from quantum statistics, hence one can ignore influence of Final State Interactions, which in this case is small. Taking into account only quantum statistics can reduce complexity of calculations and save computation time.

723 **3.2.3 Source emission function**

724 To describe particle emitting source, one uses a single emission function [26]:

725

$$S_A(\mathbf{x}_1, \mathbf{p}_1) = \int S(\mathbf{x}_1, \mathbf{p}_1, \mathbf{x}_2, \mathbf{p}_2, \dots, \mathbf{x}_N, \mathbf{p}_N) d\mathbf{x}_2 d\mathbf{p}_2 \dots d\mathbf{x}_N d\mathbf{p}_N \quad (3.6)$$

726 and a two-particle one:

$$S_{AB}(\mathbf{x}_1, \mathbf{p}_1, \mathbf{x}_2, \mathbf{p}_2) = \int S(\mathbf{x}_1, \mathbf{p}_1, \mathbf{x}_2, \mathbf{p}_2, \dots, \mathbf{x}_N, \mathbf{p}_N) d\mathbf{x}_3 d\mathbf{p}_3 \dots d\mathbf{x}_N d\mathbf{p}_N . \quad (3.7)$$

727 Emission function $S(\cdot)$ can be interpreted as a probability to emit a particle, or
 728 a pair of particles from a given space-time point with a given momentum. In
 729 principle, the source emission function should encode all physics aspects of the
 730 particle emission process i.e. the symmetrization for bosons and fermions, as
 731 well as the two-body and many body Final State Interactions. Instead of this,
 732 one assume that each particle's emission process is independent - the interac-
 733 tion between final-state particles after their creation is independent from their
 734 emission process. The assumption of this independence allows to construct two-
 735 particle emission function from single particle emission functions via a convolu-
 736 tion [26]:

$$S(\mathbf{k}^*, \mathbf{r}^*) = \int S_A(\mathbf{p}_1, \mathbf{x}_1) S_B(\mathbf{p}_2, \mathbf{x}_2) \delta \left[\mathbf{k}^* - \frac{\mathbf{p}_1 + \mathbf{p}_2}{2} \right] \delta [\mathbf{r}^* - (\mathbf{x}_1 + \mathbf{x}_2)] \times d^4 \mathbf{x}_1 d^4 \mathbf{x}_2 d^4 \mathbf{x}_1 d^3 \mathbf{p}_1 d^3 \mathbf{p}_2 \quad (3.8)$$

737 In case of identical particles, ($S_A = S_B$) several simplifications can be made. A
 738 convolution of the two identical Gaussian distributions is also a Gaussian distri-
 739 bution with σ multiplied by $\sqrt{2}$. Femtoscopy can give information only about
 740 two-particle emission function, but when considering Gaussian distribution as
 741 a source function in Eq. 3.8, one can obtain a σ of a single emission function
 742 from a two-particle emission function. The Eq. 3.8 is not reversible - an inform-
 743 ation about $S_A(\cdot)$ cannot be derived from $S_{AB}(\cdot)$. An exception from this rule
 744 is a Gaussian source function, hence it is often used in femtoscopic calculations.
 745 Considering pairs of identical particles, an emission function is assumed to be
 746 described by the following equation in the Pair Rest Frame [26]:

$$S_{1D}^{PRF}(\mathbf{r}^*) = \exp \left(-\frac{r_{out}^{*2} + r_{side}^{*2} + r_{long}^{*2}}{4R_{inv}^2} \right) . \quad (3.9)$$

To change from the three-dimensional variables to the one-dimensional variable
 one requires introduction of the proper Jacobian r^{*2} .

$$S_{1D}^{PRF}(r^*) = r^{*2} \exp \left(-\frac{r^{*2}}{4R_{inv}^2} \right) . \quad (3.10)$$

747 The “4” in the denominator before the “standard deviation” R_{inv} in the Gaussian distribution comes from the convolution of the two Gaussian distributions,
 748 which multiplies the R_{inv} by a factor of $\sqrt{2}$.

749 A more complex form of emission function was used by all RHIC and SPS experiments in identical pion femtoscopy:

$$S_{3D}^{LCMS}(\mathbf{r}) = \exp \left(-\frac{r_{out}^2}{4R_{out}^2} - \frac{r_{side}^2}{4R_{side}^2} - \frac{r_{long}^2}{4R_{long}^2} \right). \quad (3.11)$$

750 The main difference of this source function is that it has three different and independent widths R_{out} , R_{side} , R_{long} and they are defined in the LCMS, not in PRF.
 751 Unlike in PRF, in LCMS an equal-time approximation is not used. For identical
 752 particles this is not a problem - only Coulomb interaction inside a wave function
 753 depends on Δt .

755 Relationship between one-dimensional and three-dimensional source sizes

756 Up to now, most of femtoscopic measurements were limited only to averaged
 757 source size R_{av}^L (the letter “L” in superscript stands for LCMS):

$$S_{1D}^{LCMS}(\mathbf{r}) = \exp \left(-\frac{r_{out}^2 + r_{side}^2 + r_{long}^2}{2R_{av}^L} \right). \quad (3.12)$$

758 The relationship between between $S_{1D}^{LCMS}(\cdot)$ and $S_{3D}^{LCMS}(\cdot)$ is given by:

$$S_{3D}^{LCMS}(r) = \int \exp \left(-\frac{r_{out}^2}{2R_{out}^L} - \frac{r_{side}^2}{2R_{side}^L} - \frac{r_{long}^2}{2R_{long}^L} \right) \times \delta \left(r - \sqrt{r_{out}^2 + r_{side}^2 + r_{long}^2} \right) dr_{out} dr_{side} dr_{long}. \quad (3.13)$$

759 The one-dimensional source size corresponding to the three-dimensional one can
 760 be approximated by the following form:

$$S_{1D}^{LCMS}(r) = r^2 \exp \left(-\frac{r^2}{2R_{av}^L} \right). \quad (3.14)$$

761 The equation above assumes that $R_{out}^L = R_{side}^L = R_{long}^L$ hence $R_{av}^L = R_{out}^L$. If this
 762 condition is not satisfied, one can not give explicit mathematical relation between
 763 one-dimensional and three-dimensional source sizes. However, for realistic val-
 764 ues of R (i.e. for similar values of R_{out} , R_{side} , R_{long}), the S_{3D}^{LCMS} from Eq. 3.13 is
 765 not very different from Gaussian distribution and can be well approximated by
 766 Eq. 3.13.

767 A deformation of an averaged source function in case of big differences in
 768 R_{out} , R_{side} , R_{long} is presented in the Fig. 3.3. A three-dimensional Gaussian dis-
 769 tribution with varying widths was averaged into one-dimensional function using

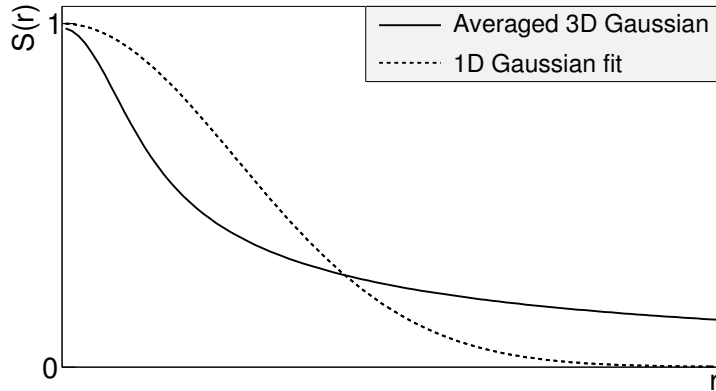


Figure 3.3: An averaged three-dimensional Gaussian source function with different widths was averaged into one-dimensional function. To illustrate deformations, one-dimensional Gaussian distribution was fitted.

770 the Eq. 3.13. Afterwards, an one-dimensional Gaussian distribution was fitted.
 771 One can notice a heavy tail of an averaged distribution in long r region, which
 772 makes an approximation using one-dimensional distribution in this case quite
 773 inaccurate.

Using Eq. 3.13 and Eq. 3.14 one can obtain a relation between one-dimensional width and the three-dimensional ones. Through numerical calculations one can find the following approximate relation [26]:

$$R_{av}^L = \sqrt{\left(R_{out}^{L^2} + R_{side}^{L^2} + R_{long}^{L^2}\right)/3}. \quad (3.15)$$

774 This equation does not depend on the pair velocity, hence it is valid in the LCMS
 775 and PRF.

776 3.2.4 Analytical form of a correlation function

777 The fundamental object in a particle interferometry is a correlation function.
 778 The correlation function is defined as:

$$C(\mathbf{p}_a, \mathbf{p}_b) = \frac{P_2(\mathbf{p}_a, \mathbf{p}_b)}{P_1(\mathbf{p}_a)P_1(\mathbf{p}_b)}, \quad (3.16)$$

779 where P_2 is a conditional probability to observe a particle with momentum \mathbf{p}_b if
 780 particle with momentum \mathbf{p}_a was also observed. A P_1 is a probability to observe
 781 a particle with a given momentum. The relationship between source emission
 782 function, pair wave function and the correlation function is described by the fol-
 783 lowing equation:

$$C(\mathbf{p}_1, \mathbf{p}_2) = \int S_{AB}(\mathbf{p}_1, \mathbf{x}_1, \mathbf{p}_2, \mathbf{x}_2) |\Psi_{AB}|^2 d^4\mathbf{x}_1 d^4\mathbf{x}_2 \quad (3.17)$$

Substituting the one-dimensional emission function (Eq. 3.10) into the integral above yields the following form of correlation function in PRF:

$$C(q) = 1 + \lambda \exp(-R_{inv}^2 q^2) \quad (3.18)$$

where q is a momentum difference between two particles. When using the three-dimensional emission function (Eq. 3.11) one gets the following correlation function defined in the LCMS:

$$C(\mathbf{q}) = 1 + \lambda \exp(-R_{out}^2 q_{out}^2 - R_{side}^2 q_{side}^2 - R_{long}^2 q_{long}^2) \quad (3.19)$$

where q_{out} , q_{side} , q_{long} are \mathbf{q} components in the outward, sideward and longitudinal direction. The λ parameter in the equations above determines correlation strength. The lambda parameter has values in the range $\lambda \in [-0.5, 1]$ and it depends on a pair type. In case of pairs of identical bosons (like $\pi\pi$ or KK) the lambda parameter $\lambda \rightarrow 1$. For identical fermions (e.g. $p-p$) $\lambda \rightarrow -0.5$. Values of λ observed experimentally are lower than 1 (for bosons) and greater than -0.5 (for fermions). There are few explanations to this effect: detector efficiencies, inclusion of misidentified particles in a used sample or inclusion of non-correlated pairs (when one or both particles come from e.g. long-lived resonance). The analysis carried out in this work uses data from a model, therefore the detector efficiency and particle purity is not taken into account [26].

3.2.5 Spherical harmonics decomposition of a correlation function

Results coming from an analysis using three-dimensional correlation function in Cartesian coordinates are quite difficult to visualize. To do that, one usually performs a projection into one dimension in outward, sideward and longitudinal directions. One may loose important information about a correlation function in this procedure, because it gives only a limited view of the full three-dimensional structure. Recently, a more advanced way of presenting correlation function - a spherical harmonics decomposition, was proposed. The three-dimensional correlation function is decomposed into an infinite set of components in a form of one-dimensional histograms $C_l^m(q)$. In this form, a correlation function is defined as a sum of a series [27]:

$$C(\mathbf{q}) = \sum_{l,m} C_l^m(q) Y_l^m(\theta, \phi), \quad (3.20)$$

where $Y_l^m(\theta, \phi)$ is a spherical harmonic function. Spherical harmonics are an orthogonal set of solutions to the Laplace's equation in spherical coordinates. Hence, in this approach, a correlation function is defined as a function of q , θ and ϕ . To obtain C_l^m coefficients in the series, one has to calculate the following integral:

$$C_l^m(q) = \int_{\Omega} C(q, \theta, \phi) Y_l^{m*}(\theta, \phi) d\Omega, \quad (3.21)$$

811 where Ω is a full solid angle.

Spherical harmonics representation has several important advantages. The main one is that it requires less statistics than traditional analysis performed in Cartesian coordinates. Another one is that it encodes full three-dimensional information in a set of one-dimensional plots. In principle it does not have to be an advantage, because full description of a correlation function requires infinite number of l, m components. But it so happens that the intrinsic symmetries of a pair distribution in a femtoscopic analysis result in most of the components to vanish. For the identical particles correlation functions, all coefficients with odd values of l and m disappear. It has also been shown, that the most significant portion of femtoscopic data is stored in the components with the lowest l values. It is expected that, the main femtoscopic information is contained in the following components [26]:

$$C_0^0 \rightarrow R_{LCMS}, \quad (3.22)$$

$$\Re C_2^0 \rightarrow \frac{R_T}{R_{long}}, \quad (3.23)$$

$$\Re C_2^2 \rightarrow \frac{R_{out}}{R_{side}}, \quad (3.24)$$

812 where $R_{LCMS} = \sqrt{(R_{out}^2 + R_{side}^2 + R_{long}^2)/3}$ and $R_T = \sqrt{(R_{out}^2 + R_{side}^2)/2}$.

813 The C_0^0 is sensitive to the overall size of a correlation function. The $\Re C_2^0$ carries
 814 the information about the ratio of the transverse to the longitudinal radii, due
 815 to its $\cos^2(\theta)$ weighting in Y_2^0 . The component $\Re C_2^2$ with its $\cos^2(\phi)$ weighting
 816 encodes the ratio between outward and sideward radii. Thus, the spherical har-
 817 monics method allows to obtain and analyze full three-dimensional femtoscopic
 818 information from a correlation function [26].

819 3.3 Experimental approach

820 The correlation function is defined as a probability to observe two particles
 821 together divided by the product of probabilities to observe each of them sepa-
 822 rately (Eq. 3.16). Experimentally this is achieved by dividing two distributions
 823 of relative momentum of pairs of particles coming from the same event and the
 824 equivalent distribution of pairs where each particle is taken from different colli-
 825 sions. In this way, one obtains not only femtoscopic information but also all other
 826 event-wide correlations. This method is useful for experimentalists to estimate
 827 the magnitude of non-femtoscopic effects. There exists also a different approach,
 828 where two particles in pairs in the second distribution are also taken from the
 829 same event. The second method gives only information about physical effects
 830 accessible via femtoscopy. The aim of this work is a study of effects coming from
 831 two particle interferometry, hence the latter method was used.

832 In order to calculate experimental correlation function, one uses the follow-
 833 ing approach. One has to construct two histograms: the *numerator* N and the

834 denominator D with the particle pairs momenta, where particles are coming from
 835 the same event. Those histograms can be one-dimensional (as a function of $|\mathbf{q}|$),
 836 three dimensional (a function of three components of \mathbf{q} in LCMS) or a set of one-
 837 dimensional histogram representing components of the spherical harmonic de-
 838 composition of the distribution. The second histogram, D is filled for each pair
 839 with the weight 1.0 at a corresponding relative momentum $\mathbf{q} = 2\mathbf{k}^*$. The first one,
 840 N is filled with the same procedure, but the weight is calculated as $|\Psi_{ab}(\mathbf{r}^*, \mathbf{k}^*)|^2$.
 841 A division N/D gives the correlation function C . This procedure can be simply
 842 written as [26]:

$$C(\mathbf{k}^*) = \frac{N}{D} = \frac{\sum_{n_i \in D} \delta(\mathbf{k}_i^* - \mathbf{k}^*) |\Psi_{ab}(\mathbf{r}_i^*, \mathbf{k}_i^*)|^2}{\sum_{n_i \in D} \delta(\mathbf{k}_i^* - \mathbf{k}^*)} . \quad (3.25)$$

The D histogram represents the set of all particle pairs used in calculations.
 The n_i is a pair with the its relative momentum \mathbf{k}_i^* and relative separation \mathbf{r}_i^* .
 Mathematically, the procedure of calculating the Eq. 3.25 is equivalent to a
 calculation of an integral in Eq. 3.17 through a Monte-Carlo method. The wave
 function used in Eq. 3.25 has one of the following forms:

$$|\Psi_{\pi\pi}(\mathbf{r}^*, \mathbf{k}^*)|^2 = |\Psi_{KK}(\mathbf{r}^*, \mathbf{k}^*)|^2 = 1 + \cos(2\mathbf{k}^* \mathbf{r}^*) , \quad (3.26)$$

$$|\Psi_{pp}(\mathbf{r}^*, \mathbf{k}^*)|^2 = 1 - \frac{1}{2} \cos(2\mathbf{k}^* \mathbf{r}^*) . \quad (3.27)$$

843 The first one is used in case of bosons, and the latter one is for identical fermions.
 844 A wave function for pair of spin-1/2 fermions (Eq. 3.27) is a superposition of two
 845 possible states: singlet state (with spin equal to 0 and one eigenstate) and triplet
 846 state (with spin equal to 1 and three possible eigenstates). For a singlet state, a
 847 wave function is symmetric, and for triplet state, it is antisymmetric. In other
 848 words the $|\Psi_{pp}|^2$ encodes correlation coming from Bose-Einstein statistics (with
 849 weight 1/4) and anti-correlation from Fermi-Dirac distribution (with weight 3/4).

850 3.4 Scaling of femtoscopy radii

851 A particle interferometry formalism presented in the previous sections as-
 852 sumes that particle emitting source is static. This is not the case in heavy ion
 853 collisions at LHC. An existence of transverse radial and elliptic flow suggest that
 854 created system is dynamic. To address this issue, a concept of *lengths of homogen-*
 855 *eity* was introduced. It is defined as:

$$\frac{|f(p, x + \lambda) - f(p, x)|}{f(p, x)} = 1 , \quad (3.28)$$

856 where λ is the homogeneity length. It can be interpreted as the distance at which
 857 relative change of the source Wigner function f becomes large. One can measure

the lengths of homogeneity of a system using femtoscopic radii. This concept can be intuitively explained on a basis of hydrodynamic models. Each source element is emitting particles with a velocity which is a combination of two components: a fluid cell velocity β_f (which is taken from the flow field $u_\mu(x^\mu)$) and thermal velocity β_{th} (which has random direction). These particles can combine into pairs of small relative momenta and become correlated. If two particles are emitted far ($|x_a - x_b| > \lambda$) away from each other, the flow field u_μ in their point of emission might be very different and it will be impossible for them to have sufficiently small relative momenta to be in the region of interference effect. This effect is presented in Fig. 3.4. An increase of a correlation is visible for pairs with low relative momenta [8].

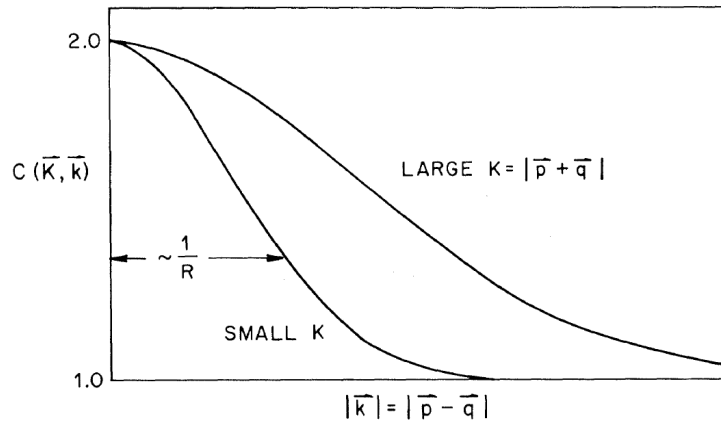


Figure 3.4: Correlation function width dependence on total pair momentum. Pion pairs with a large total momentum have a wider correlation (smaller apparent source) [28].

868

869 3.4.1 Scaling in LCMS

Hydrodynamic calculations performed in LCMS show that femtoscopic radii in outward, sideward, and longitudinal direction show dependence on transverse mass $m_T = \sqrt{k_T^2 + m^2}$, where m is a mass of a particle [29]. Moreover, experimental results show that this scaling is observed for R_{LCMS} radii also. This dependence can be expressed as follows:

$$R_i = \alpha m_T^{-\beta} \quad (3.29)$$

870 where i subscript indicates that this equation applies to R_{out} , R_{side} and R_{long}
871 radii. The β exponent is approximately equal 0.5. In case of strong transversal
872 expansion of the emitting source, the decrease of longitudinal interferometry ra-
873 dius can be more quick than $m_T^{-0.5}$, hence one can expect for longitudinal radii
874 greater values of $\beta > 0.5$ [29].

875 **3.4.2 Scaling in PRF**

876 In the collisions at the LHC energies, pions are most abundant particles and
 877 their multiplicities are large enough to enable three-dimensional analysis. How-
 878 ever, for heavier particles, such as kaons and protons statistical limitations arise.
 879 Hence it is often possible to only measure one-dimensional direction-averaged
 880 radius R_{inv} for those particles. The R_{inv} is then calculated in the PRF. The trans-
 881 ition from LCMS to PRF is a Lorentz boost in the direction of pair transverse
 882 momentum with velocity $\beta_T = p_T/m_T$. Hence only R_{out} changes:

$$R_{out}^* = \gamma_T R_{out}. \quad (3.30)$$

883 A Lorentz factor $\gamma_T = m_T/m$ depends on the particle type, therefore for the
 884 lighter particles (and for the same m_T) γ_T is much larger, which causes bigger
 885 growth of R_{out} and overall radius. This transformation to PRF breaks the scaling
 886 observed in the LCMS radii.

887 This increase of radius in the outward direction induces overall source
 888 size growth and whatsoever the source distribution function becomes
 889 non-gaussian. In this case the source function is developing long-range tails and
 890 its one-dimensional projection is much narrower than Gaussian distribution.
 891 This deformation is presented in Fig. 3.3. The influence of these effects can be
 892 expressed with an approximate formula:

$$R_{inv} = \sqrt{(R_{out}^2 \sqrt{\gamma_T} + R_{side}^2 + R_{long}^2)/3}. \quad (3.31)$$

893 Because the averaging of the radii is done in quadrature, one would have expec-
 894 ted appearance of γ_T^2 instead of $\sqrt{\gamma_T}$ in this equation. However the Monte-Carlo
 895 procedure shows that this is not the case and the actual growth is smaller than
 896 the naive expectation. Numerical simulations yield that this increase is best de-
 897 scribed with the $\sqrt{\gamma_T}$ in the Eq. 3.31 [30].

Assuming that radii in all directions are equal $R_{out} = R_{side} = R_{long}$, Eq. 3.31
 can be reverted using Eq. 3.15 to express relationship between LCMS and PRF
 overall radii [30]:

$$R_{LCMS} \approx R_{inv} \times [(\sqrt{\gamma_T} + 2)/3]^{-1/2}. \quad (3.32)$$

898 This approximate formula allows to restore power-law behaviour of the scaled
 899 radii not only when the radii are equal, but also when their differences are small
 900 (for explanation see the last part of the Section 3.2.3).

901 This method of recovering scaling in PRF can be used as a tool for the search
 902 of hydrodynamic collectivity between pions, kaons and protons in heavy ion col-
 903 lisions with the measurement of one-dimensional radius in PRF.

904 **Chapter 4**

905 **Results**

906 For the purposes of the femtosopic analysis in this thesis, the THERMINATOR
907 model was used to generate large number of events for eight different sets of
908 initial conditions corresponding the following centrality ranges: 0-5%, 0-10%,
909 10-20%, 20-30%, 30-40%, 40-50%, 50-60% and 60-70% for the Pb-Pb collisions at
910 the centre of mass energy $\sqrt{s_{NN}} = 2.76$ TeV. Software used in the process of
911 calculating correlation functions is described in Appendix A. Plots in this chapter
912 were generated using macros described in Appendix C.

913 **4.1 Identical particles correlations**

914 The correlation functions (three-dimensional and one-dimensional) were cal-
915 culated separately for the following different pairs of identical particles: π - π , K -
916 K and p - p for nine k_T bins (in GeV/c): 0.1-0.2, 0.2-0.3, 0.3-0.4, 0.4-0.5, 0.6-0.7,
917 0.7-0.8, 0.8-1.0 and 1.0-1.2. In case of kaons, k_T ranges start from 0.3 and for pro-
918 tons from 0.4 and for both of them the maximum value is 1.0. The k_T ranges for
919 the heavier particles were limited to maintain sufficient multiplicity to perform
920 reliable calculations.

921 **4.1.1 Spherical harmonics components**

922 The three-dimensional correlation function as a function of relative
923 momentum q_{LCMS} was calculated in a form of components of spherical
924 harmonics series accordingly to the Eq. 3.21. In the femtosopic analysis of
925 identical particles, the most important information is stored in the $\Re C_0^0$, $\Re C_2^0$
926 and $\Re C_2^2$, hence only those components were analyzed. Correlation functions
927 obtained in this procedure were calculated for the different centrality bins for the
928 pairs of pions, kaons and protons. They are presented in the Fig. 4.1, 4.2 and 4.3.

929 Coefficients for pairs of identical bosons (pions and kaons) are shown
930 in the Fig. 4.1 and 4.2. The wave function symmetrization (Bose-Einstein
931 statistics) causes the increase of a correlation in the low relative momenta

regime ($q_{LCMS} < 0.06 \text{ GeV/c}$ or even $q_{LCMS} < 0.12 \text{ GeV/c}$ for more peripheral collisions). It is clearly visible in the $\Re C_0^0$ component. The $\Re C_0^0$ resembles one-dimensional correlation function and in the sense that it encodes information about the overall source radius. The second coefficient $\Re C_2^0$ differs from zero (is negative), which yields the information about the ratio R_T/R_{long} . The $\Re C_2^2$ stores the information about R_{out}/R_{side} ratio and one can notice that it is non-vanishing (is also negative).

The correlation function for a pair of identical fermions is presented in the Fig. 4.3. A wave function for a pair of protons is a composition of singlet (described by Bose-Einstein statistics) and triplet state (described by the

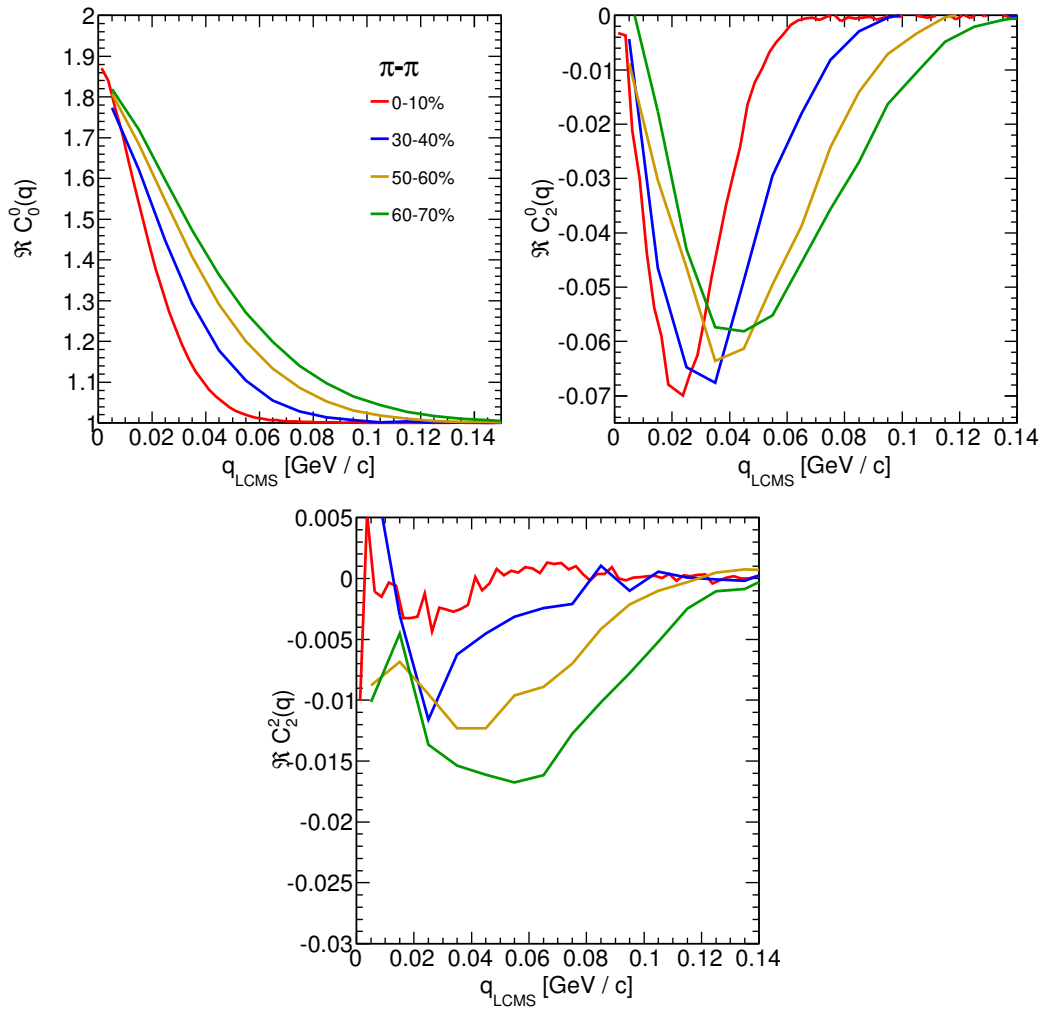


Figure 4.1: Spherical harmonics coefficients of the two-pion correlation function. From the top left: $\Re C_0^0$, $\Re C_2^0$ and $\Re C_2^2$. Only few centrality bins are presented for increased readability.

942 Fermi-Dirac statistics - see Section 3.3). An influence of Fermi-Dirac statistics has
 943 its effect in the decrease of a correlation down to 0.5 at low relative momentum
 944 ($q_{LCMS} < 0.1 \text{ GeV/c}$ or $q_{LCMS} < 0.15 \text{ GeV/c}$ for more peripheral collisions),
 945 which can be observed in $\Re C_0^0$. The $\Re C_2^0$ and $\Re C_2^2$ coefficients differ from zero
 946 and are becoming positive.

947 The common effect of the spherical harmonics form of a correlation function
 948 is the “mirroring” of the shape of the $\Re C_0^0$ coefficient - when correlation func-
 949 tion increases at low q_{LCMS} , the $\Re C_2^0$ and $\Re C_2^2$ are becoming negative and vice
 950 versa. This is quite different behaviour than in the case of correlations of non-

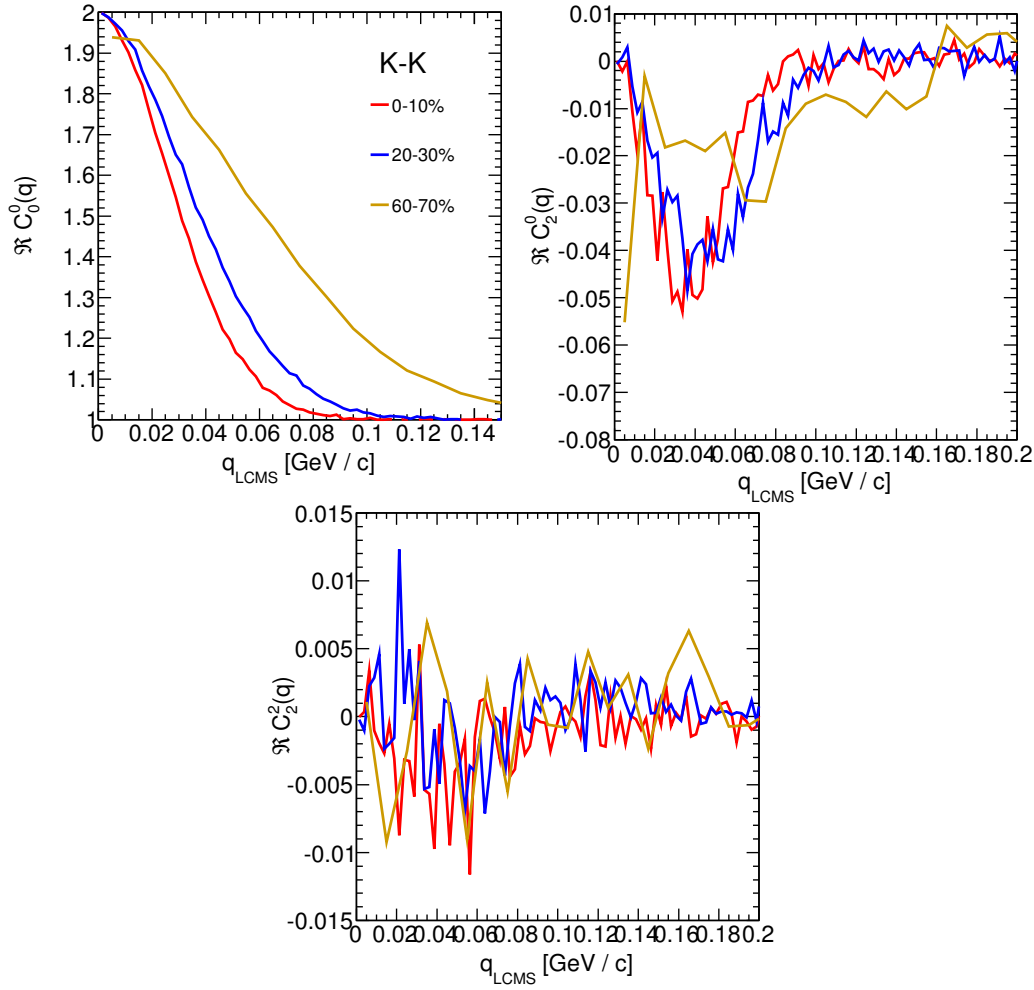


Figure 4.2: Spherical harmonics coefficients of the two-kaon correlation function. From the top left: $\Re C_0^0$, $\Re C_2^0$ and $\Re C_2^2$. Only few centrality bins are presented for increased readability. The $\Re C_2^2$ is noisy, but one can still notice that it differs from zero and is becoming negative.

951 identical particles, where the $\Re C_2^0$ still behaves in the same manner, but $\Re C_2^2$ has
 952 the opposite sign to the $\Re C_2^0$ [26].

953 In all cases, the correlation function gets wider with the peripherality of a
 954 collision i.e. the correlation function for most central collisions (0-10%) is much
 955 narrower than for the most peripheral ones (60-70%). This phenomena is clearly
 956 visible the $\Re C_0^0$ coefficients. Other components are also affected by this effect,
 957 this is especially noticeable in the case of kaons and pions. For the protons, the
 958 results are noisy, hence this effect is not clearly distinguishable.

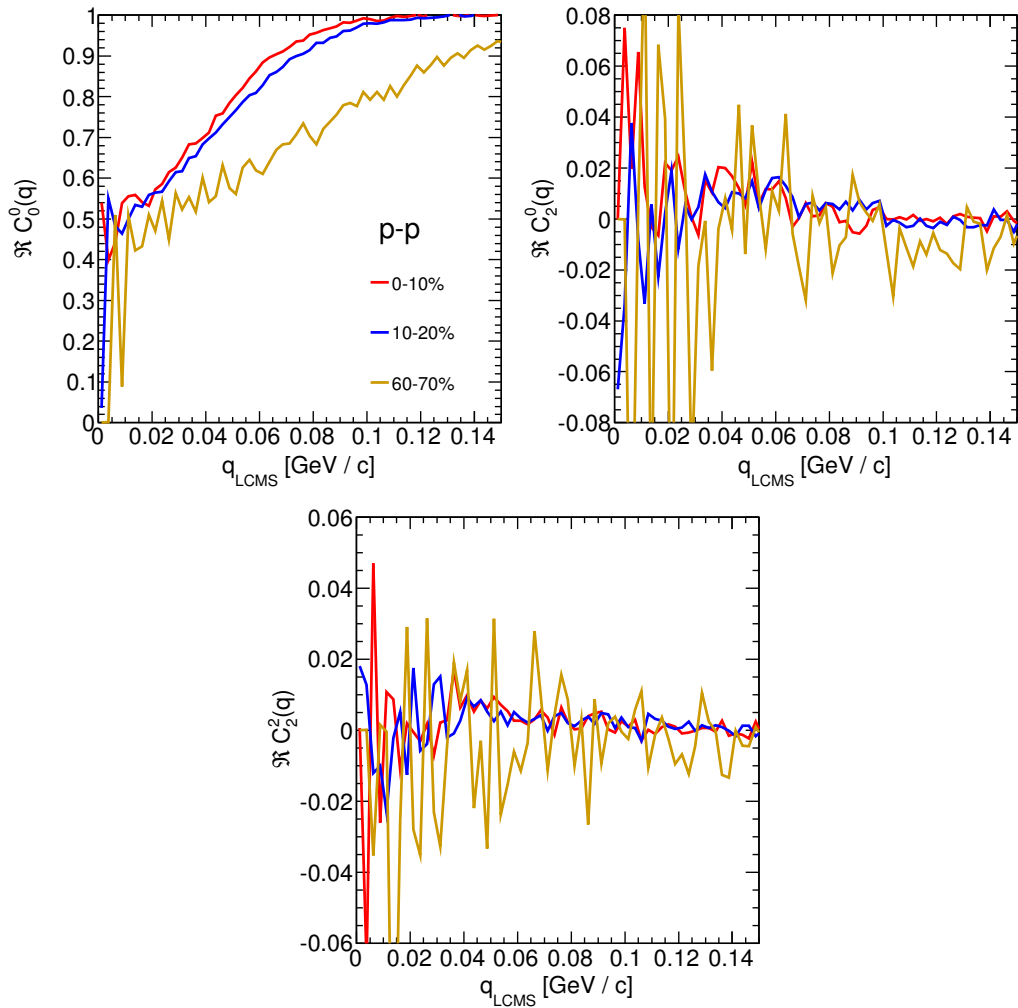


Figure 4.3: Spherical harmonics coefficients of the two-proton correlation function. From the top left: $\Re C_0^0$, $\Re C_2^0$ and $\Re C_2^2$. Only few centrality bins are presented for increased readability. The $\Re C_2^0$ and $\Re C_2^2$ are noisy, but one can still notice, that they differ from zero and are becoming positive.

959 **4.1.2 Centrality dependence of a correlation function**

960 The centrality dependence of a correlation function is especially visible in
961 one-dimensional correlation functions. This effect is presented in the Fig. 4.4 -
962 the correlation functions for pions, kaons and protons are plotted for the same
963 k_T range but different centrality bins. One can notice that the width of a func-
964 tion is smaller in the case of most central collisions. Hence, the femtoscopic radii
965 (proportional to the inverse of width) are increasing with the centrality. An ex-
966 planation for this growth is that in the most central collisions, a size of a created
967 system is larger than for the peripheral ones.

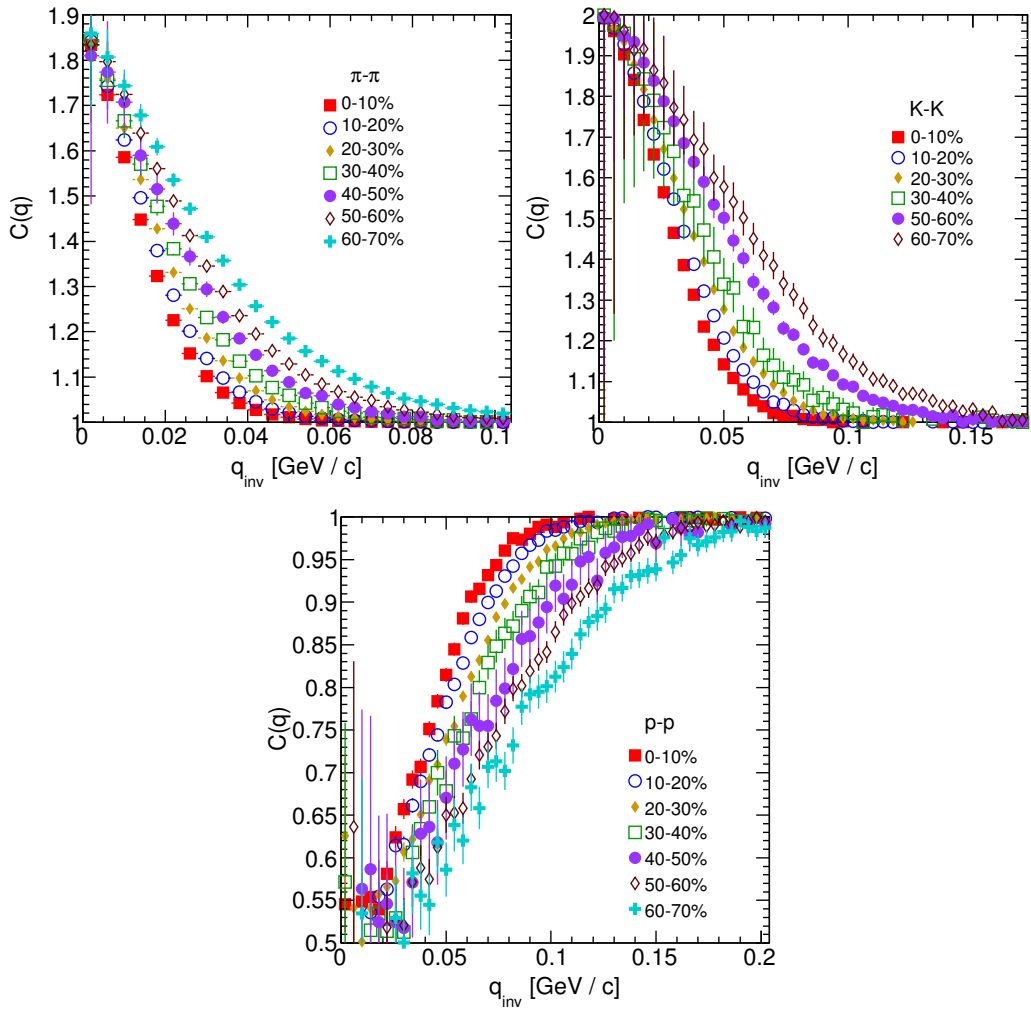


Figure 4.4: One-dimensional correlation function for pions (top left), kaons (top right) and protons (bottom) for different centralities.

4.1.3 k_T dependence of a correlation function

In the Fig. 4.5 there are presented one-dimensional correlation functions for pions, kaons and protons for the same centrality bin, but different k_T ranges. One can observe in all cases of the particle types, appearance of the same trend: with the increase of the total transverse momentum of a pair, the width of a correlation function increases and the femtoscopic radius decreases. The plots in the Fig. 4.5 were zoomed in to show the influence of k_T .

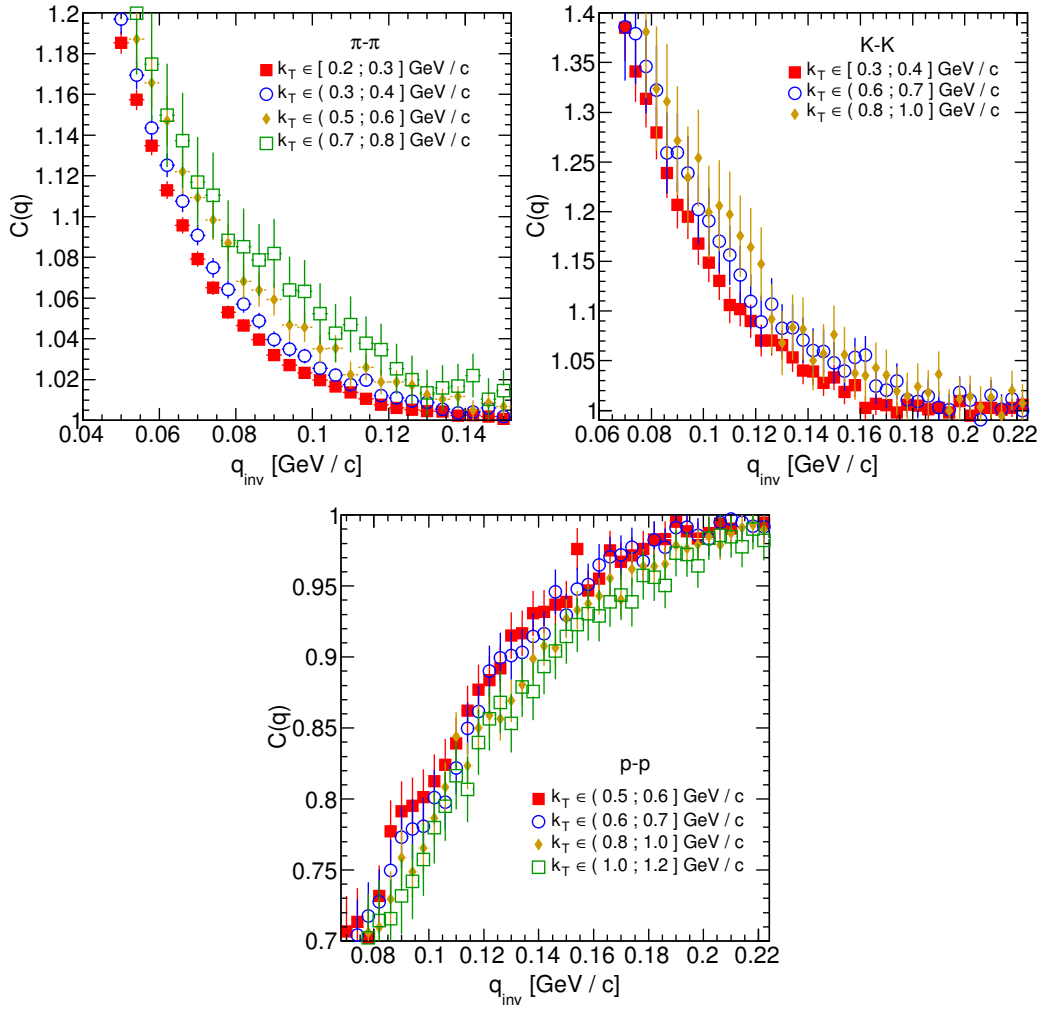


Figure 4.5: One-dimensional correlation functions for pions, kaons and protons, for the same centrality bin and different k_T ranges. The plot was zoomed in to the region which illustrates the k_T dependence in the best way. Only few of the calculated ranges are presented for better readability.

4.2 Results of the fitting procedure

In order to perform a quantitative analysis of a wide range of correlation functions, the theoretical formulas were fitted to the calculated experimental-like data. In this procedure, the femtoscopic radii for the three-dimensional as well as one-dimensional correlation functions were extracted. The main goal of this analysis is a verification of a common transverse mass scaling for different particles types. Obtained radii are plotted as a function of a transverse mass $m_T = \sqrt{k_T^2 + m^2}$. To test the scaling, the following power-law was fitted to the particular radii afterwards:

$$R_x = \alpha m_T^{-\beta}, \quad (4.1)$$

where the α and β are free parameters. The procedure of fitting and used software are described in Appendix B.

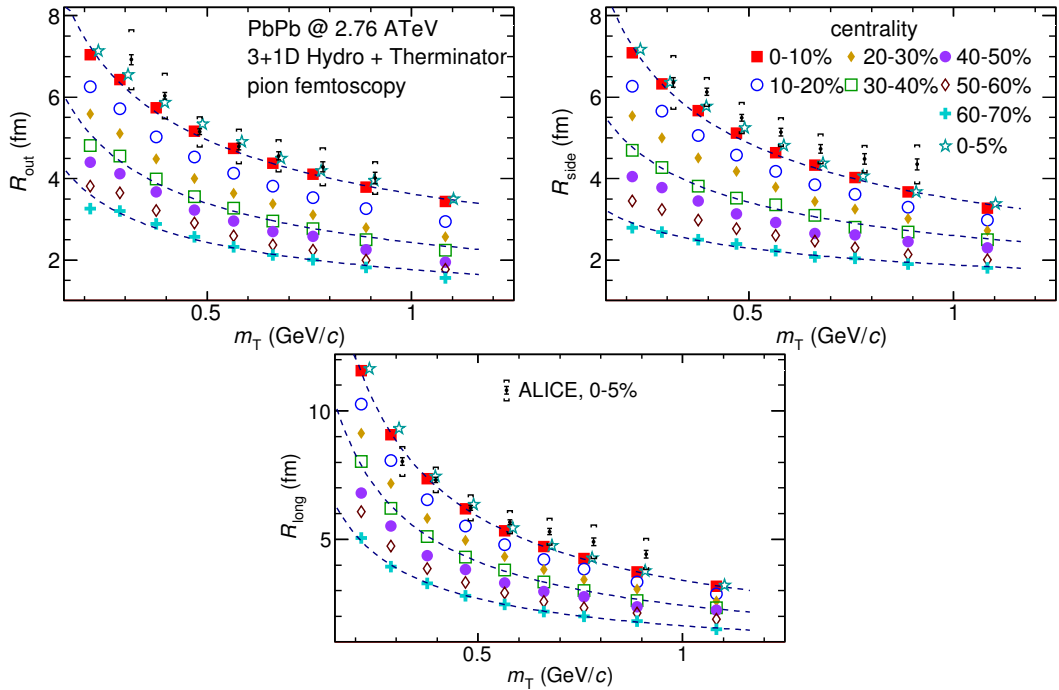


Figure 4.6: Femtoscopic radii in LCMS coming from two-pion correlation functions for all centrality bins as a function of m_T . The dashed lines are power-law fits. The most central collisions (0-5%) are compared to the results from ALICE [31]. The two datasets are shifted to the right for visibility [30].

4.2.1 The three-dimensional femtoscopic radii scaling

The femtoscopic radii in the outward, sideward and longitudinal directions for the analysis of two-pion correlation functions in the LCMS are presented in Fig. 4.6. The dashed lines are fits of the power law to the data. One can notice, that the power law describes data points well with a 5% accuracy. The β fit parameter for the outward direction is in the order of 0.45. For the sideward direction, this parameter has the similar value, but it is lower for the most peripheral collisions. In case of the longitudinal direction, the β has greater value, up to 0.75. In the Fig. 4.6, results for the top 5% central collisions (star-shaped markers) with experimental data from ALICE [31] are also compared. The experimental results are consistent with the ones coming from the model predictions.

The Fig. 4.7 presents femtoscopic radii coming from the kaon calculations. The R_{out} , R_{side} and R_{long} fall also with the power-law within the 5% accuracy. The β parameter was larger in case of kaons: 0.59 in outward direction, 0.54 in the sideward and 0.86 for longitudinal.

The results for two-proton analysis are shown in the Fig. 4.8. The Eq. 4.1 was fitted to the data and tells that the protons also follow the m_T scaling within 5% range. The β parameter values were even bigger for the outward (0.58),

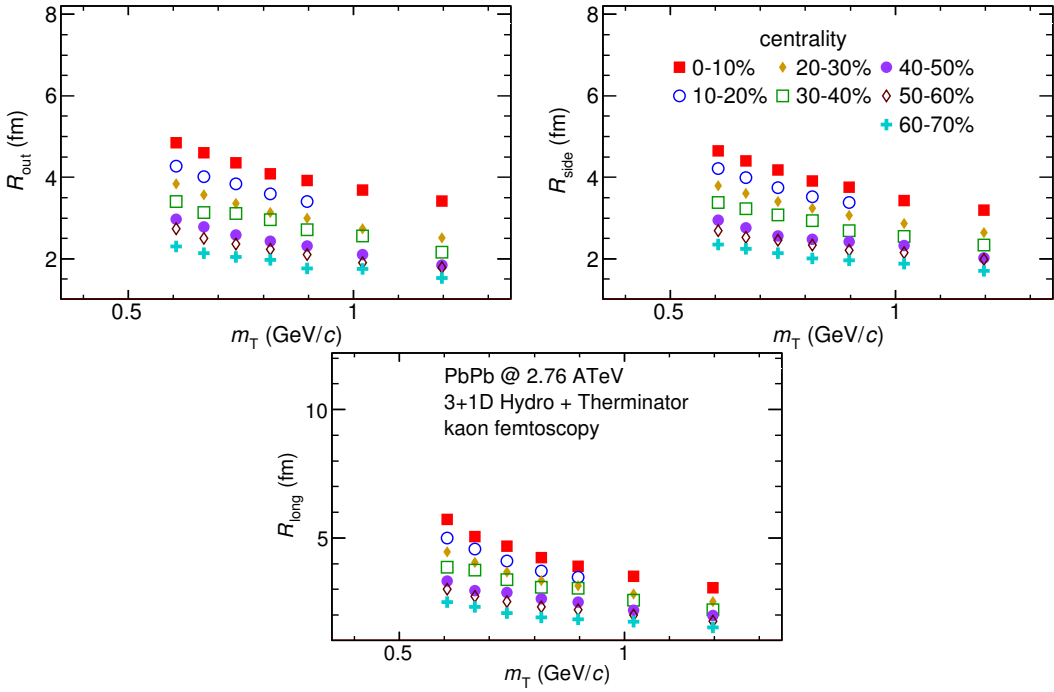


Figure 4.7: Femtoscopic radii extracted from two-kaon correlation functions for different centrality bins as a function of m_T . [30].

1005 sideward (0.61) and longitudinal (1.09) directions than for the other particle
 1006 types.

1007 The Fig. 4.9 presents results for the pions, kaons and protons together as a
 1008 function of m_T . Considering differences in the β value for the fits for differ-
 1009 ent particles, one can suspect that there is no common scaling between different
 1010 kinds of particles. However, when all of the results shown on the same plot, they
 1011 are aligning on the common curve and the scaling is well preserved. The scaling
 1012 accuracy is 3%, 5% and 4% for the 0-10%, 20-30% and 60-70% for the outward
 1013 direction. For the sideward radii the scaling is better, with average deviations
 1014 2%, 2% and 3% respectively. In case of longitudinal direction the accuracy is 6%,
 1015 5% and 3% for the three centralities. The β parameter for the outward direction is
 1016 close to 0.42 in all cases. For the sideward direction it varies from 0.28 to 0.47 and
 1017 is bigger for more central collisions. Regarding longitudinal radii, the exponent
 1018 is bigger than the other two: $\beta \in [0.62; 0.72]$. Considering all results, the plotted
 1019 radii are following the common power-law scaling within the 5% accuracy for all
 1020 directions, centralities and particle types.

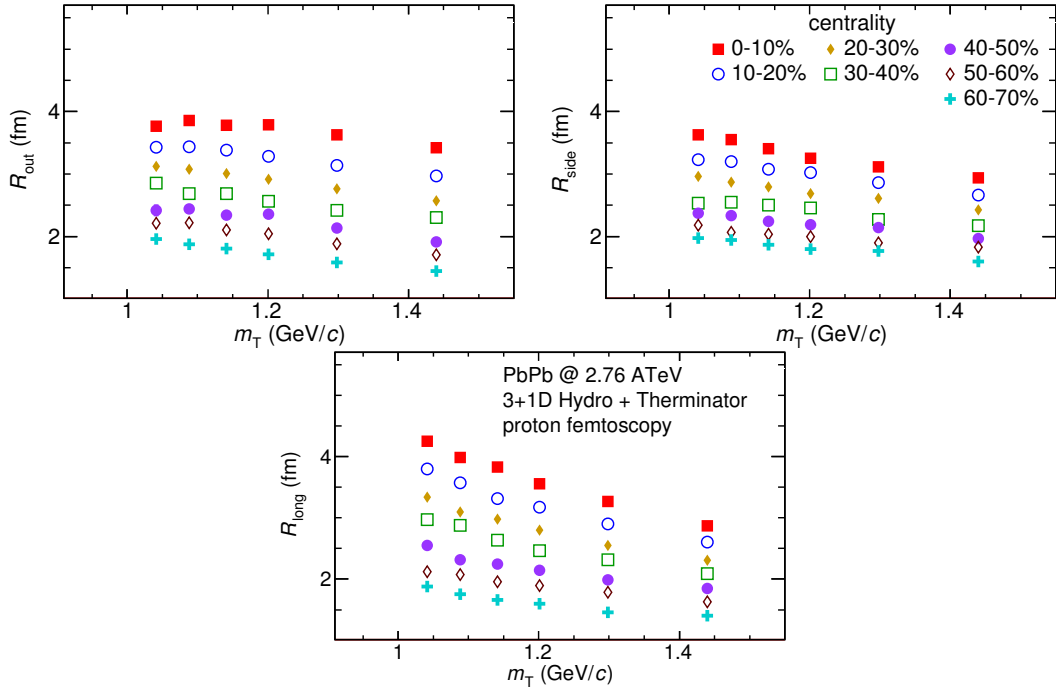


Figure 4.8: Femtoscopic radii extracted from two-proton correlation functions for different centrality bins as a function of m_T . [30].

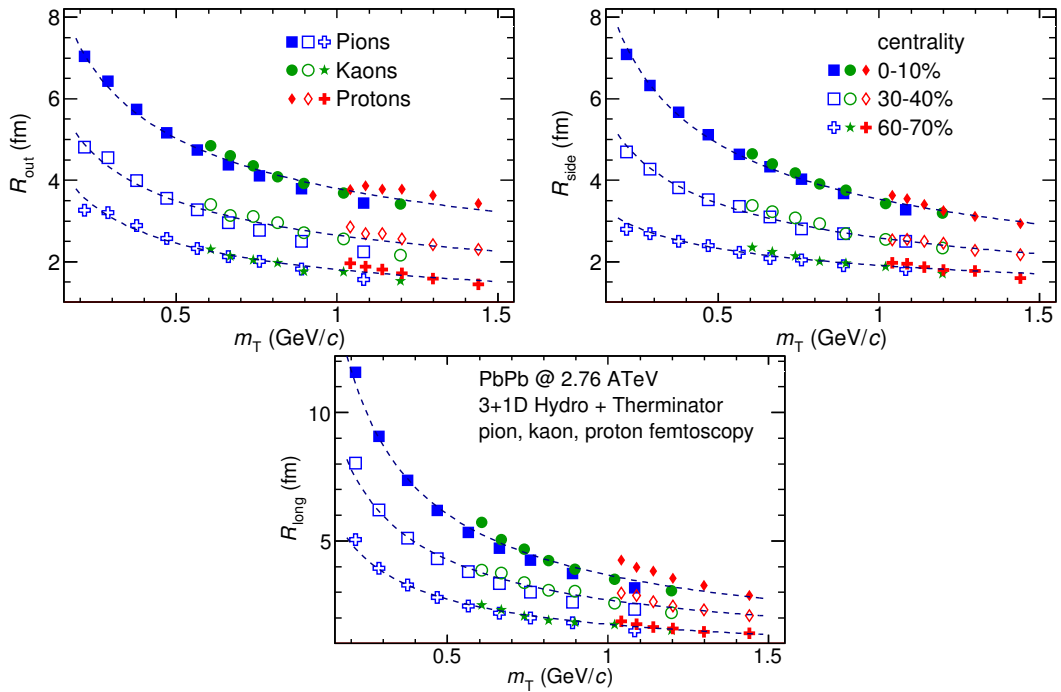


Figure 4.9: The results from the calculations for the pions, kaons and protons in for the three centralities presented on the common plot. One can notice that radii for particular centralities and different particle types follow the common power-law scaling. [30].

1021 **4.2.2 Scaling of one-dimensional radii**

1022 To the one-dimensional correlation function, the corresponding function in
 1023 the PRF given by the Eq. 3.18 was fitted. The results from those fits are presented
 1024 in the upper left plot in the Fig. 4.10. One immediately notices, that there is no
 1025 common scaling of R_{inv} for different kind of particles. In Fig. 4.9 the radii in the
 1026 outward direction for the pions, kaons and protons for the same m_T are similar.
 1027 However, when one performs a transition from the LCMS to the PRF, the R_{out}
 1028 radius grows:

$$R_{out}^* = \gamma_T R_{out}, \quad (4.2)$$

1029 where $\gamma_T = m_T/m$. For the lighter particles, the γ_T is much larger, hence the
 1030 bigger growth of the R_{out} and the overall radius. This is visible in the Fig. 4.10
 1031 (top left), where the radii in the PRF for the lighter particles are bigger than for
 1032 the heavier ones in case of the same m_T range.

1033 In the Fig. 4.9 there is visible scaling in the outward, sideward and longitudi-
 1034 nal direction. Hence one can expect an appearance of such scaling in a direction-
 1035 averaged radius calculated in the LCMS. This radius is presented in the Fig. 4.10
 1036 (bottom) and indeed the R_{LCMS} exhibits power-law scaling with m_T .

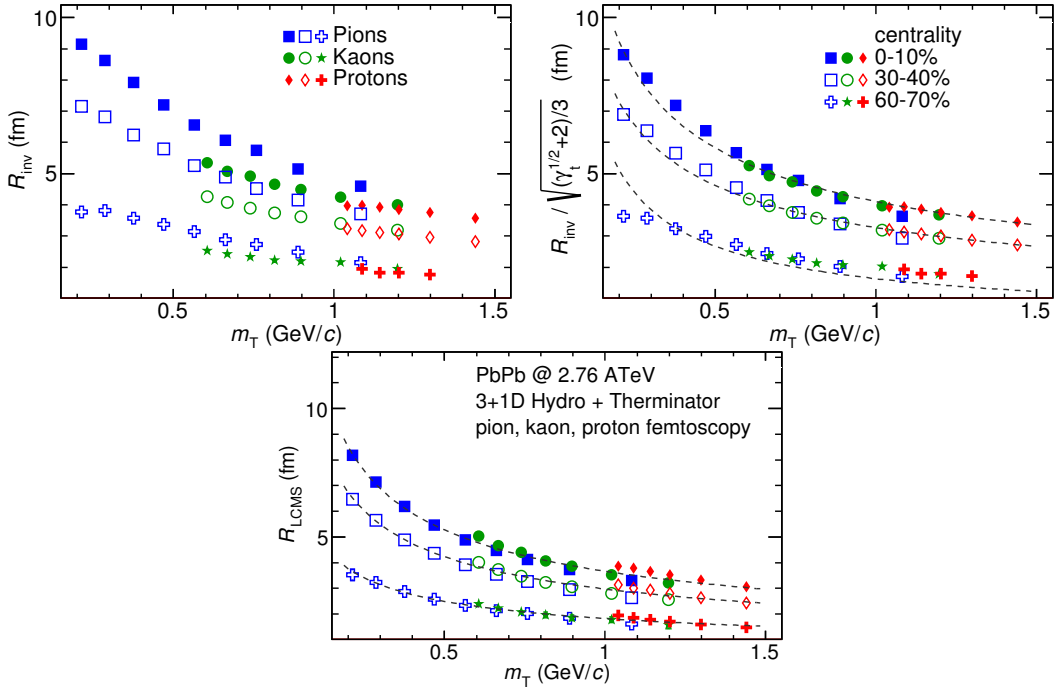


Figure 4.10: Top left: one-dimensional radius for pions, kaons and protons calculated in the PRF. Top right: the R_{inv} scaled by the proposed factor. Bottom: averaged one-dimensional radius in the LCMS for pions, kaons and protons. Only three centrality bins are shown for the better readability [30].

1037 One can try to account the effect of an increase of the radii in the outward direction
 1038 by using the appropriate scaling factor. In Fig. 4.10 (top right), femtoscopic
 1039 radii in the LCMS are divided by the proposed scaling factor:

$$f = \sqrt{(\sqrt{\gamma_T} + 2)/3} . \quad (4.3)$$

1040 The radii for pions, kaons and protons in the PRF after the division by f are
 1041 following the power-law with the accuracy of 10%.

1042 4.3 Discussion of the results

1043 The femtoscopic radii obtained from the three-dimensional correlation func-
 1044 tion fitting exhibit the m_T dependence described by the power law (Eq. 4.1). This
 1045 scaling is preserved quite well with accuracy <10%. Observation of such scaling
 1046 in a femtoscopic radii is a strong signal of the appearance of a collective beha-
 1047 viour of a particle-emitting source created in the collision. The data used in the
 1048 analysis was coming from the hydrodynamic model, hence one can indeed ex-
 1049 pect the appearance of this scaling. However, the results for pion femtoscopy
 1050 from the ALICE at LHC are consistent with the data from analysis performed in
 1051 this thesis (Fig. 4.6). This is a confirmation of an applicability of hydrodynamic
 1052 models in a description of an evolution of a quark-gluon plasma.

1053 The β parameter calculated in the fitting of the power-law to the femtoscopic
 1054 radii is of the order of 0.5 in case of the radii in the transverse plane. This value is
 1055 consistent with the hydrodynamic predictions. In case of longitudinal radii, the
 1056 exponent is bigger (greater than 0.7), which is an indication of a strong transversal
 1057 expansion in the system [29].

1058 A scaling described above is visible in the LCMS, however due to limited
 1059 statistics, analysis in this reference frame is not always possible. In such case
 1060 one performs calculations in the PRF. The m_T scaling in the PRF is not observed
 1061 - this has a trivial kinematic origin. A transition from the PRF to LCMS causes
 1062 growth of the radius in the outward direction and the common power-law scal-
 1063 ing for different particles breaks due to differences in the $\gamma_T(m_T)$ for different
 1064 particle types. However one can try to deal with the radius growth and restore
 1065 the scaling by dividing the radii R_{inv} by an approximate factor $\sqrt{(\sqrt{\gamma_T} + 2)/3}$.
 1066 The scaled R_{inv} are following the power-law and could be used as a verification
 1067 of hydrodynamic behaviour in the investigated particle source.

1068 The hadronic evolution and freeze-out in the THERMINATOR is followed by
 1069 the resonance propagation and decay phase. A good accuracy of a scaling with
 1070 the power-law indicated that the inclusion of the resonances does not break the
 1071 m_T scaling. However, recent calculations, which include also hadron rescatter-
 1072 ing phase, indicate that the scaling between pions and kaons is broken at the
 1073 LHC [32]. Thus, the results of this work suggest that the scaling breaks at the
 1074 hadron rescattering phase [30].

¹⁰⁷⁵ Conclusions

¹⁰⁷⁶ This thesis presents the results of the two-particle femtoscopy of different
¹⁰⁷⁷ particle kinds produced in Pb-Pb collisions at the centre of mass energy
¹⁰⁷⁸ $\sqrt{s_{NN}} = 2.76$ TeV. The analysed data was generated by the THERMINATOR
¹⁰⁷⁹ model using hypersurfaces from (3+1)-dimensional hydrodynamic calculations.

¹⁰⁸⁰ The momentum correlations were studied for three different types of particle
¹⁰⁸¹ pairs: pions, kaons and protons. The data was analyzed for eight different sets of
¹⁰⁸² initial conditions corresponding the following centrality ranges: 0-5%, 0-10%, 10-
¹⁰⁸³ 20%, 20-30%, 30-40%, 40-50%, 50-60% and 60-70%. The correlation functions were
¹⁰⁸⁴ calculated for nine k_T bins from 0.1 GeV/c to 1.2 GeV/c. The calculations were
¹⁰⁸⁵ performed using spherical harmonics decomposition of a three-dimensional cor-
¹⁰⁸⁶ relation function. Using this approach, one can obtain full three-dimensional
¹⁰⁸⁷ information about the source size using only the three coefficients: $\Re C_0^0$, $\Re C_2^0$
¹⁰⁸⁸ and $\Re C_2^2$. To perform further quantitative analysis, the femtoscopic radii were
¹⁰⁸⁹ extracted through fitting.

¹⁰⁹⁰ The calculated correlation functions show expected increase of a correlation
¹⁰⁹¹ at low relative momenta in case of identical bosons (pions and kaons) and the
¹⁰⁹² decrease for the identical fermions (protons) respectively. This effect is especially
¹⁰⁹³ visible in the first spherical harmonic coefficient $\Re C_0^0$. The other two components
¹⁰⁹⁴ $\Re C_2^0$ and $\Re C_2^2$ are non-vanishing and are providing information about the ratios
¹⁰⁹⁵ of radii in the outward, sideward and longitudinal directions.

¹⁰⁹⁶ An increase of width of a correlation function with the peripherality of a colli-
¹⁰⁹⁷ sion and the k_T is observed for pions, kaons and protons. This increase of femto-
¹⁰⁹⁸scopic radii (proportional to the inverse of width) with k_T is related with the m_T
¹⁰⁹⁹ scaling predicted by the hydrodynamic calculations.

¹¹⁰⁰ Hydrodynamic equations are predicting appearance of the common scaling
¹¹⁰¹ of femtoscopic radii for different kinds of particles with $m_T^{-0.5}$ in the LCMS. In
¹¹⁰² the results of this work, a common scaling for different particle types is observed
¹¹⁰³ in LCMS in the outward, sideward and longitudinal direction. The direction-
¹¹⁰⁴ averaged radius R_{LCMS} also shows this power-law behaviour. The fitting of a
¹¹⁰⁵ power law $\alpha m_T^{-\beta}$ to the femtoscopic radii yielded the information, that the β
¹¹⁰⁶ exponent for the outward and sideward direction is of the order of 0.5, which is
¹¹⁰⁷ consistent with the hydrodynamic predictions. For the longitudinal direction, the
¹¹⁰⁸ β is bigger (>0.7) than in the other directions which is an indication of a strong
¹¹⁰⁹ transverse flow. Femtoscopic radii in LCMS are following the power-law scaling

1110 with the accuracy <5% for pions and kaons, and <10% in case of protons.

1111 In case of the one-dimensional radii R_{inv} calculated in the PRF, no common
1112 scaling is observed. This is a consequence of a transition from the LCMS to the
1113 PRF, which causes the growth of radius in the outward direction and breaks the
1114 scaling for different particles. However, one can try to correct the influence of
1115 the R_{out} growth with an approximate factor $\sqrt{(\sqrt{\gamma_T} + 2)/3}$. After the division
1116 of the R_{inv} by the proposed factor, the scaling is restored with an accuracy <10%.
1117 In this way, the experimentally simpler measure of the one-dimensional radii can
1118 be used as a probe for the hydrodynamic collectivity.

1119 The THERMINATOR model includes hydrodynamic expansion, statistical had-
1120 ronization, resonance propagation and decay afterwards. The m_T scaling is pre-
1121 dicted from the pure hydrodynamic calculations. However, this study shows,
1122 that influence of the resonances on this scaling is less than 10%.

1123 **Appendix A**

1124 **Scripts for correlation function
calculations**
1125

1126 **A.1 Events generation**

1127 In order to perform analysis with sufficient statistics, a big number of events is
1128 required. To handle this task, a computer cluster at Faculty of Physics at Warsaw
1129 University of Technology was used. This cluster consists of 20 nodes with the fol-
1130 lowing hardware configuration: Intel® Core™ 2 Quad CPU Q6600 @ 2.40GHz,
1131 8GB RAM with Scientific Linux 5.8. The communication between nodes is real-
1132 ized by the TORQUE Resource Manager [33]. To control process of launching
1133 multiple event generators and collecting the data, the following scripts were writ-
1134 ten using Bash scripting language:

1135 **skynet.sh** This is a script in a form of a batch job for TORQUE. It simply
1136 launches multiple THERMINATOR processes in the same working directory
1137 with the separate output folders for each job. This solution has two
1138 advantages: saves space and computation time. First of all, a single
1139 freeze-out hypersurface file has size about 230 MB. This approach allows
1140 to avoid time- and space-consuming copying of the whole THERMINATOR
1141 directory before running the application. Thus, in the case of running 20
1142 instances of this generator, it makes significant difference. The second
1143 advantage is a possibility to share files containing information about
1144 particles' multiplicities and maximum integrands between generator
1145 processes (more detailed description is presented in Section 2.3). One can
1146 simply execute this batch job using the following command:

1147 `qsub -q long -t 0-19 skynet.sh -v dir=th_5.7,events=6000`
1148 It adds 20 event generators (with task ids from 0 to 19) to the queue,
1149 sets the THERMINATOR directory as `th_5.7` and a number of simulated
1150 events to 6000 for each process. This command should be executed in the
1151 directory one level higher than `th_5.7` folder.

1152 **merge_events.sh** After the generation process, one has to merge calculated
 1153 events into one directory. This task requires renaming of a large number of
 1154 THERMINATOR event files. Each event generator job produces files named
 1155 with a certain pattern, starting from event000.root with increasing number.
 1156 In order to move the event files and preserve continuity in the numbering,
 1157 a simple script was written. An example of use:

1158 `find /data/source -iname "event*.root" -type f \`
 1159 `| merge_events.sh`

1160 This command will find all the event files in the folder /data/source,
 1161 move and rename them accordingly to the numeration of events in the
 1162 current working directory.

1163 Sources of these two scripts are available on-line at <https://github.com/carbolymer/msc/tree/master/alix>.

1165 A.2 Calculations of experimental-like correlation 1166 functions

1167 Correlation functions utilized in this analysis were calculated using `tpi`
 1168 software written by Adam Kisiel and designed for reading event files from
 1169 THERMINATOR. It uses ROOT library for calculations and storage of the data.
 1170 This application provides functionality of calculation of one-dimensional
 1171 correlation functions in PRF, three-dimensional one in LCMS and its spherical
 1172 harmonics decomposition (see Section 3.2.5). The exact numerical procedure of
 1173 computation of a correlation function is presented in Section 3.3. `tpi` allows to
 1174 perform calculations with the following options:

- 1175 • Pair type - there are pion-pion, kaon-kaon, proton-proton and many more
 1176 pairs available (including ones consisting of non-identical particles)
- 1177 • Multiple k_T subranges from 0.21 to 1.2 GeV/c
- 1178 • Possibility to include Coulomb interaction
- 1179 • Number of events to mix
- 1180 • Maximum freeze-out time
- 1181 • Choice of method of background calculation in correlation function (mixing
 1182 events or using particles from the same event)

1183 This program generates results in the *.root files format in a form of histograms.
 1184 Output file contains numerators, denominators and correlation functions from
 1185 one-dimensional and three-dimensional analyses. Moreover, the spherical har-
 1186 monics series coefficients up to $l = 3$ with signal and background histograms are
 1187 stored.

1188 **Appendix B**

1189 **Fitting utilities**

1190 Procedure of fitting analytical formulas to experimental-like correlation func-
1191 tions was performed using custom software written in C++ and Bash. This ap-
1192 plication utilizes MINUIT [34] package built in the ROOT library.

1193 The source of fitting software is available on-line at [https://github.com/
1194 carbolymer/msc/tree/master/fitting](https://github.com/carbolymer/msc/tree/master/fitting).

1195 **B.1 Minuit package**

1196 The MINUIT is a physics analysis tool for function minimization written in
1197 Fortran programming language. This tool was designed for statistical analysis
1198 and it is working on χ^2 or log-likelihood functions to compute the best-fit para-
1199 meter values and uncertainties, including correlations between parameters. It is
1200 implemented in ROOT environment as TMinuit class, which provides interface
1201 to the minimization tool. The analysis performed in this work uses MINUIT with
1202 the Migrad minimization method. The Migrad minimizer is the best one embed-
1203 ded in Minuit. It is a variable-metric method with inexact line search, a stable
1204 metric updating scheme, and checks for positive-definiteness [34].

1205 **B.2 Fitting software**

1206 Fitting application provides tools for extraction of femtoscopic radii from cor-
1207 relation functions for identical particles. It also provides a macro for generating
1208 plots with radii as a function of transverse mass and fitting power-law $\alpha m_T^{-\beta}$ to
1209 the results.

1210 **B.2.1 Input parameters**

1211 The application reads the output files from the tpi program and extracts
1212 from them one-dimensional and three-dimensional correlation functions. The
1213 latter ones are in a form of spherical harmonics series coefficients.

The program gives a possibility to set fit parameters for certain centrality bins, pair types and k_T ranges. Configuration files (*.conf) are located inside the application's folder in the data/ directory. Files with the names beginning with *fitsh* contain parameters for three-dimensional fits, while *fit1d* prefix indicates settings for one-dimensional ones. In principle, names of the parameter files are following this pattern: *{fit type}.{centrality}.{pair type}.{kT range beginning}.conf*, for example: *fit1d.b3.1.pp.0.6.conf*. To set parameters for all fits of the same kind of particles, one has to create file with the following name: *{fit type}.{pair type}.conf*. For example, *fitsh.kk.conf* file contains initial parameters for all fits for kaon pairs. Similarly, one can set fit parameters for pions (*ppi*) and protons correlation functions (*pp*) using corresponding letters in place of *kk* in the name of the file.

1225 An example content of configuration file for one-dimensional fit (**fit1d**) is
1226 presented below:

1.0	L	normalization
1.0	L	λ
4.0	L	R_{inv}
0.0	F	not used

1227 The *F* letter after the parameter indicates fixed value (will not change during
1228 fitting process), whereas the *L* parameter tells that this value will be modified.

1229 An example configuration file for three-dimensional fit (`fitsh`):

0.0 F 0.0 0.0	not used
0.0 F 0.0 0.0	not used
IdLCYlm	correlation function numerator name
0.0075	beginning of the fitting range (q in GeV/c)
0.2	end of the fitting range (q in GeV/c)
0	not used

1230 This file contains extra columns specify allowed range for the value of a fit
 1231 parameter. The minimum of the range is determined by the value in the 3rd
 1232 column, while the 4th column contains its maximum.

1233 **B.2.2 Output format**

1234 The application during calculations creates subdirectories for each centrality
 1235 inside the `data/` directory. For each pair type and each of the following variables
 1236 R_{inv} , R_{out} , R_{side} , R_{long} , λ and R_{LCMS} , the output files `*.out` with four columns are
 1237 created. First column is the beginning of the k_T range, while the second one is its
 1238 end, third column contains result of the fit and the last one stores uncertainty of
 1239 this value. In addition, plots (in the png format) of the correlation functions for
 1240 each pair type and k_T bin are generated inside subdirectories.

1241 Files `filelist.{pair type}.in` include list of input `*.root` files with processed corre-
 1242 lation functions.

1243 **B.2.3 Compilation**

1244 This utility requires ROOT framework and `libboost-regex-dev` library.
 1245 Compilation can be performed using `make` command inside application's dir-
 1246 ectory.

1247 **B.2.4 Usage**

1248 **Fitting process**

1249 In order to start the fitting process, one should execute the following com-
 1250 mand:

1251 `./run.sh /path/to/the/tpi/output centrality`

1252 The `/path/to/the/tpi/output` parameter is a location of tpi output files
 1253 and `centrality` is a name of a directory, where the fitting results will be stored.

1254 Plotting

1255 In order to plot femtoscopic radii and perform fitting of power law, one has
1256 to use the following command:

1257 make plots

1258 Plots will be generated in the output directory.

1259 **Appendix C**

1260 **Plotting scripts**

1261 **C.1 Correlation functions plots**

1262 Plots containing correlation functions were generated using two ROOT macros
1263 written in C++.

1264 The first one, **cf1DAllCentralities.C** generates two plots with one-dimen-
1265 sional correlation functions. One of them presents k_T dependence of a correlation
1266 function (saved in the *cfvskt.eps* file), while the other one shows influence of
1267 centrality on a correlation function (saved in the *cfvsctr.eps* file). In order to gener-
1268 ate plots, one has to set in the line 9 the path to the folder including subdirectories
1269 with correlation functions files. One can produce eps files, using the following
1270 command:

1271 `root -l -b -q cf1DAllCentralities.C`

1272 *cfvskt.eps* and *cfvsctr.eps* files will be generated in the current working directory.

1273 The second macro, **cf3DAllCentralities.C** produces plots with spherical har-
1274 monics coefficients for pions (*cf3dpi.eps*), kaons (*cf3dk.eps*) and protons (*cf3dp.eps*).
1275 This script has similar structure to the previous one. Like in the previous case,
1276 one also has to set the proper path in the line 18. To execute this macro, one can
1277 use this command:

1278 `root -l -b -q cf3DAllCentralities.C`

1279 As a result, the three files with the output plots will be generated in the current
1280 working directory.

1281 The sources of these plotting macros are available on-line at <https://github.com/carbolymer/msc/tree/develop/fitting/macros>.

1283 **C.2 Plots with femtoscopy radii**

1284 Femtoscopy radii plots can be generated using fitting tool described in Ap-
1285 pendix B. To do so, one has to invoke the following command:

1286 `make plots`

1287 This command executes ROOT macro *src/plotter.C* which generates all plots for the

every centrality automatically. This script for every pair type, k_T and centrality bin reads the femtoscopic radii and calculates the transverse mass. Afterwards, to all of the femtoscopic radii as a function of transverse mass, the following formula is fitted: $R_x = \alpha m_T^{-\beta}$. It should be noted, that the fitting is performed to the radii of pions, kaons and protons together. As a result of this process, plot with femtoscopic radii in the outward, sideward, and longitudinal direction as well as overall radii is generated for every centrality. Moreover, the comparison between different centralities in PRF divided by the scaling factor (see Section 3.4) and the R_{LCMS} are also plotted.

¹²⁹⁷ Bibliography

- ¹²⁹⁸ [1] Standard Model of Elementary Paticles - Wikipedia, the free encyclopedia
¹²⁹⁹ http://en.wikipedia.org/wiki/Standard_Model.
- ¹³⁰⁰ [2] R. Aaij et al. (LHCb Collaboration). Observation of the resonant character of
¹³⁰¹ the $z(4430)^-$ state. *Phys. Rev. Lett.*, 112:222002, Jun 2014.
- ¹³⁰² [3] Donald H. Perkins. *Introduction to High Energy Physics*. Cambridge University Press, fourth edition, 2000. Cambridge Books Online.
- ¹³⁰⁴ [4] G. Odyniec. *Phase Diagram of Quantum Chromo-Dynamics* - course at Faculty
¹³⁰⁵ of Physics, Warsaw University of Technology, Jun 2012.
- ¹³⁰⁶ [5] J. Beringer et al. (Particle Data Group). The Review of Particle Physics. *Phys.*
¹³⁰⁷ *Rev.*, D86:010001, 2012.
- ¹³⁰⁸ [6] Z. Fodor and S.D. Katz. The Phase diagram of quantum chromodynamics.
¹³⁰⁹ 2009.
- ¹³¹⁰ [7] F. Karsch. Lattice results on QCD thermodynamics. *Nuclear Physics A*, 698(1-
¹³¹¹ 4):199 – 208, 2002.
- ¹³¹² [8] Adam Kisiel. *Studies of non-identical meson-meson correlations at low relative ve-*
¹³¹³ *locities in relativistic heavy-ion collisions registered in the STAR experiment*. PhD
¹³¹⁴ thesis, Warsaw University of Technology, Aug 2004.
- ¹³¹⁵ [9] J. Bartke. *Relativistic Heavy Ion Physics*. World Scientific Pub., 2009.
- ¹³¹⁶ [10] W. Florkowski. *Phenomenology of Ultra-Relativistic Heavy-Ion Collisions*.
¹³¹⁷ World Scientific, 2010.
- ¹³¹⁸ [11] Science Grid This Week, October 25, 2006 - Probing the Perfect Liquid with
¹³¹⁹ the STAR Grid [http://www.interactions.org/sgtw/2006/1025/](http://www.interactions.org/sgtw/2006/1025/star_grid_more.html)
¹³²⁰ [star_grid_more.html](http://www.interactions.org/sgtw/2006/1025/star_grid_more.html).
- ¹³²¹ [12] K. Grebieszkow. Fizyka zderzeń ciężkich jonów, <http://www.if.pw.edu.pl/~kperl/HIP/hip.html>.
- ¹³²³ [13] Ulrich W. Heinz. From SPS to RHIC: Maurice and the CERN heavy-ion
¹³²⁴ programme. *Phys.Scripta*, 78:028005, 2008.

- 1325 [14] J. Adams et al. Identified particle distributions in pp and Au+Au collisions
1326 at $s_{\text{NN}}^{**}(1/2) = 200 \text{ GeV}$. *Phys.Rev.Lett.*, 92:112301, 2004.
- 1327 [15] G. David, R. Rapp, and Z. Xu. Electromagnetic Probes at RHIC-II. *Phys.Rept.*,
1328 462:176–217, 2008.
- 1329 [16] A. Marin et al. Dilepton measurements with CERES. *PoS*, CPOD07:034,
1330 2007.
- 1331 [17] J. Adams et al. Experimental and theoretical challenges in the search for the
1332 quark gluon plasma: The STAR Collaboration’s critical assessment of the
1333 evidence from RHIC collisions. *Nucl.Phys.*, A757:102–183, 2005.
- 1334 [18] Adam Kisiel, Tomasz Taluc, Wojciech Broniowski, and Wojciech
1335 Florkowski. THERMINATOR: THERMal heavy-IoN generATOR. *Comput.Phys.Commun.*, 174:669–687, 2006.
- 1337 [19] Mikolaj Chojnacki, Adam Kisiel, Wojciech Florkowski, and Wojciech Bro-
1338 niowski. THERMINATOR 2: THERMal heavy IoN generATOR 2. *Comput.
1339 Phys.Commun.*, 183:746–773, 2012.
- 1340 [20] ROOT - A Data Analysis Framework <http://root.cern.ch/drupal/>.
- 1341 [21] I. et al (BRAHMS Collaboration) Bearden. Charged meson rapidity distri-
1342 butions in central Au + Au collisions at $\sqrt{s_{\text{NN}}} = 200 \text{ GeV}$. *Phys. Rev. Lett.*,
1343 94:162301, Apr 2005.
- 1344 [22] W. Israel and J.M. Stewart. Transient relativistic thermodynamics and kin-
1345 etic theory. *Annals of Physics*, 118(2):341 – 372, 1979.
- 1346 [23] Piotr Bożek. Flow and interferometry in (3 + 1)-dimensional viscous hydro-
1347 dynamics. *Phys. Rev. C*, 85:034901, Mar 2012.
- 1348 [24] K. Kovtun, P. D. T. Son, and A. O. Starinets. Viscosity in strongly interacting
1349 quantum field theories from black hole physics. *Phys. Rev. Lett.*, 94:111601,
1350 Mar 2005.
- 1351 [25] Fred Cooper and Graham Frye. Single-particle distribution in the hydro-
1352 dynamic and statistical thermodynamic models of multiparticle production.
1353 *Phys. Rev. D*, 10:186–189, Jul 1974.
- 1354 [26] Adam Kisiel. Nonidentical-particle femtoscopy at $\sqrt{s_{\text{NN}}} = 200 \text{ GeV}$ in hy-
1355 drodynamics with statistical hadronization. *Phys. Rev. C*, 81:064906, Jun
1356 2010.
- 1357 [27] Adam Kisiel and David A. Brown. Efficient and robust calculation of femto-
1358 scopic correlation functions in spherical harmonics directly from the raw
1359 pairs measured in heavy-ion collisions. *Phys.Rev.*, C80:064911, 2009.

- 1360 [28] S. Pratt. Pion Interferometry for Exploding Sources. *Phys.Rev.Lett.*, 53:1219–
1361 1221, 1984.
- 1362 [29] S.V. Akkelin and Yu.M. Sinyukov. The HBT-interferometry of expanding
1363 inhomogeneous sources. *Z.Phys.*, C72:501–507, 1996.
- 1364 [30] A. Kisiel, M. Galazyn, and P. Bozek. Pion, kaon, and proton femtoscopy in
1365 Pb–Pb collisions at $\sqrt{s_{NN}}=2.76$ TeV modeled in 3+1D hydrodynamics. 2014.
- 1366 [31] K. Aamodt et al. Two-pion Bose-Einstein correlations in central Pb-Pb colli-
1367 sions at $\sqrt{s_{NN}} = 2.76$ TeV. *Phys.Lett.*, B696:328–337, 2011.
- 1368 [32] V.M. Shapoval, P. Braun-Munzinger, Iu.A. Karpenko, and Yu.M. Sinyukov.
1369 Femtoscopy correlations of kaons in $Pb + Pb$ collisions at LHC within hy-
1370 drokinetic model. 2014.
- 1371 [33] TORQUE Resource Manager - An open source resource manager provid-
1372 ing control over batch jobs and distributed compute nodes <http://www.adaptivecomputing.com/products/open-source/torque/>.
- 1373
- 1374 [34] MINUIT - Function Minimization and Error Analysis <http://wwwasdoc.web.cern.ch/wwwasdoc/minuit/minmain.html>.
- 1375

¹³⁷⁶ List of Figures

1377 1.1	The Standard Model of elementary particles [1].	3
1378 1.2	A string breaking and a creation of a new quark-anti-quark pair [4].	5
1379 1.3	The coupling parameter α_s dependence on four-momentum transfer Q^2 [5].	6
1380 1.4	The QCD potential for a quark-antiquark pair as a function of distance for different temperatures. A value of a potential decreases with the temperature [4].	7
1381 1.5	A number of degrees of freedom as a function of a temperature [7].	7
1382 1.6	Phase diagram coming from the Lattice QCD calculations [8]. . . .	8
1383 1.7	Left: stages of a heavy ion collision simulated in the UrQMD model. Right: schematic view of a heavy ion collision evolution [8].	9
1384 1.8	Overlapping region which is created in heavy ion collisions has an almond shape. Visible x-z plane is a <i>reaction plane</i> . The x-y plane is a <i>transverse plane</i> . The z is a direction of the beam [11].	11
1385 1.9	Cross-section of a heavy ion collision in a transverse plane. The b parameter is an <i>impact parameter</i> - a distance between centers of nuclei during a collision. An impact parameter is related with the centrality of a collision and a volume of the quark-gluon plasma [12].	12
1386 1.10	<i>Lower:</i> The elliptic flow v_2 follows the hydrodynamical predictions for an ideal fluid perfectly. Note that > 99% of all final hadrons have $p_T < 1.5 \text{ GeV}/c$. <i>Upper left:</i> The v_2 plotted versus transverse kinetic energy $KE_T = m_T - m_0 = \sqrt{p_T^2 + m_0^2} - m_0$. The v_2 follows different universal curves for mesons and baryons. <i>Upper right:</i> When scaled by the number of valence quarks, the v_2 follows the same universal curve for all hadrons and for all values of scaled transverse kinetic energy [13].	13
1387 1.11	Invariant yield of particles versus transverse mass $m_T = \sqrt{p_T^2 + m_0^2}$ for π^\pm , K^\pm , p and \bar{p} at mid-rapidity for p+p collisions (bottom) and Au+Au events from 70-80% (second bottom) to 0-5% (top) centrality [14].	14

1407	1.12 Thermal photons spectra for the central Au+Au collisions at $\sqrt{s_{NN}} = 200$ GeV computed within different hydrodynamical models compared with the pQCD calculations (solid line) and experimental data from PHENIX (black dots) [15].	15
1411	1.13 Left: Invariant mass spectrum of e^+e^- pairs in Pb+Au collisions at 158A GeV compared to the sum coming from the hadron decays predictions. Right: The expectations coming from model calculations which assume a drop of the ρ mass (blue) or a spread of the ρ width in the medium (red) [16].	16
1416	1.14 Azimuthal angle difference $\Delta\phi$ distributions for different colliding systems at $\sqrt{s_{NN}} = 200$ GeV. Transverse momentum cut: $p_T > 2$ GeV. For the Au+Au collisions the away-side jet is missing [17]. . .	17
1419	2.1 The cascade decay in the single freeze-out model. An unstable resonance x_N is formed at the freeze-out hypersurface and travels for the time τ_N depending on its lifetime and decays. If the products are also resonances (x_{N-1}, x_2) they decay further until the stable particles are formed (x_1) [18].	24
1424	3.1 Bertsch-Pratt direction naming convention used in heavy ion collision.	26
1426	3.2 The pair wave function is a superposition of all possible states. In case of particle interferometry it includes two cases: particles with momenta p_1, p_2 registered by detectors A, B and p_1, p_2 registered by B, A respectively.	27
1430	3.3 An averaged three-dimensional Gaussian source function with different widths was averaged into one-dimensional function. To illustrate deformations, one-dimensional Gaussian distribution was fitted.	30
1434	3.4 Correlation function width dependence on total pair momentum. Pion pairs with a large total momentum have a wider correlation (smaller apparent source) [28].	34
1437	4.1 Spherical harmonics coefficients of the two-pion correlation function. From the top left: $\Re C_0^0$, $\Re C_2^0$ and $\Re C_2^2$. Only few centrality bins are presented for increased readability.	37
1440	4.2 Spherical harmonics coefficients of the two-kaon correlation function. From the top left: $\Re C_0^0$, $\Re C_2^0$ and $\Re C_2^2$. Only few centrality bins are presented for increased readability. The $\Re C_2^2$ is noisy, but one can still notice that it differs from zero and is becoming negative.	38

1444	4.3 Spherical harmonics coefficients of the two-proton correlation function. From the top left: $\Re C_0^0$, $\Re C_2^0$ and $\Re C_2^2$. Only few centrality bins are presented for increased readability. The $\Re C_2^0$ and $\Re C_2^2$ are noisy, but one can still notice, that they differ from zero and are becoming positive.	39
1445		
1446		
1447		
1448		
1449	4.4 One-dimensional correlation function for pions (top left), kaons (top right) and protons (bottom) for different centralities.	40
1450		
1451		
1452		
1453		
1454		
1455		
1456	4.5 One-dimensional correlation functions for pions, kaons and protons, for the same centrality bin and different k_T ranges. The plot was zoomed in to the region which illustrates the k_T dependence in the best way. Only few of the calculated ranges are presented for better readability.	41
1457		
1458		
1459		
1460		
1461	4.6 Femtoscopic radii in LCMS coming from two-pion correlation functions for all centrality bins as a function of m_T . The dashed lines are power-law fits. The most central collisions (0-5%) are compared to the results from ALICE [31]. The two datasets are shifted to the right for visibility [30].	42
1462		
1463		
1464		
1465	4.7 Femtoscopic radii extracted from two-kaon correlation functions for different centrality bins as a function of m_T . [30].	43
1466		
1467		
1468	4.8 Femtoscopic radii extracted from two-proton correlation functions for different centrality bins as a function of m_T . [30].	44
1469		
1470	4.9 The results from the calculations for the pions, kaons and protons in for the three centralities presented on the common plot. One can notice that radii for particular centralities and different particle types follow the common power-law scaling. [30].	45
1471		
1472		
1473	4.10 Top left: one-dimensional radius for pions, kaons and protons calculated in the PRF. Top right: the R_{inv} scaled by the proposed factor. Bottom: averaged one-dimensional radius in the LCMS for pions, kaons and protons. Only three centrality bins are shown for the better readability [30].	46